PCCP

PAPER

View Article Online
View Journal | View Issue

Open Access Article. Published on 30 March 2020. Downloaded on 2/8/2026 12:45:32 PM.
This article is licensed under a Creative Commons Attribution 3.0 Unported Licence.

Cite this: *Phys. Chem. Chem. Phys.*, 2020, **22**, 7912

Received 27th January 2020,
Accepted 9th March 2020

DOI: 10.1039/d0cp00443j

rsc.li/pccp

Charge separation and successive reconfigurations of electronic and protonic states in a water-splitting catalytic cycle with the Mn_4CaO_5 cluster. On the mechanism of water splitting in PSII†

Kentaro Yamamoto and Kazuo Takatsuka*

Much insight into the basic mechanisms of photoexcited and collision-induced ground-state water splitting has been accumulated in our nonadiabatic electron wavepacket dynamics studies based on a building-block approach reaching up to systems of binuclear Mn oxo complexes. We here extend the study to a ground-state water-splitting catalytic cycle with tetranuclear Mn oxo complex Mn_4CaO_5, or $Mn_3Ca(H_2O)_2(OH)_4–OH–Mn^{(4)}(H_2O)_2$, where $Mn_3Ca(H_2O)_2(OH)_4$ is fixed to a skewed cubic structure by μ-hydroxo bridges and is tied to the terminal group $Mn^{(4)}(H_2O)_2$. We show using the method of real-time nonadiabatic electron wavepacket dynamics that four charge separation steps always take place only through the terminal group $Mn^{(4)}(H_2O)_2$ alone, thereby producing 4 electrons and 4 protons which are transported to the acceptors. Each of the three charge separation steps is followed by a reloading process from the skewed cubic structure, by which electrons and protons are refilled to the vacant terminal group so that the next charge separation dynamics can resume. After the fourth charge separation an oxygen molecule is generated. It is emphasized that the mechanisms of O_2 generation should depend on the multiple channels of reloading.

1 Introduction

Photoinduced water-splitting

$$2H_2O + 4h\nu \rightarrow 4H^+ + 4e^- + O_2 \qquad (1)$$

is a fundamental process of conversion of photon energy into some other form such as chemical energy. As for water-splitting in photosystem II (PSII), complete understanding of the catalytic cycle with the Mn_4CaO_5 cluster being the unique catalyst is one of the ultimate goals.[1–10] Yet there are still quantum mechanical mysteries involved despite many experimental and theoretical studies. For technological applications of photoinduced water-splitting (see for example ref. 11–16), not only oxides of various numbers of Mn atoms but also other elements are frequently studied as efficient catalysts. In any water-splitting scheme, the main products should be protons and electrons, and oxygen molecules and/or peroxides as a possible precursor of O_2 are by-products produced as a result of charge separation $H^+ + e^-$ in water splitting. (In fact, there is a type of photosynthesis in nature, called anoxygenic photosynthesis, which does not emit O_2.) For biological systems, peroxides are particularly harmful and are desired not to be produced.

A major difference between biological and artificial water-splitting systems is that the catalytic reaction of the former is widely believed to take place in the electronic ground state of Mn_4CaO_5, while the catalysts used in the latter are usually directly photoexcited. The main characteristics of these types of splitting are summarized in Table 1, which shows the essential differences between the mechanisms.

It is quite natural to conceive that the water-splitting cycle is triggered and driven by four charge separation dynamics. Besides, it is known that even a mononuclear Mn oxo complex can induce charge separation by itself. However, it alone does not constitute a catalytic cycle. Therefore we have been scrutinizing the dynamics of charge separation by increasing the number of Mn atoms in the oxide complex and/or proton–electron acceptors step by step in order to identify what chemical processes are essential and to see what follows the charge separation dynamics, which should eventually lead to oxygen generation before completing the catalytic cycle. Such a building-block approach, or bottom-up approach, by means of a nonadiabatic electron wavepacket study has recently reached a photo-catalytic cycle with binuclear Mn oxo complexes.[17–22] We here extend the study to a ground-state water-splitting catalytic cycle in terms of a tetranuclear Mn oxo complex.

Fukui Institute for Fundamental Chemistry, Kyoto University, Sakyou-ku, Kyoto 606-8103, Japan. E-mail: kyamamoto@fukui.kyoto-u.ac.jp, kaztak@fukui.kyoto-u.ac.jp

† Electronic supplementary information (ESI) available. See DOI: 10.1039/d0cp00443j

This journal is © the Owner Societies 2020

Open Access Article. Published on 30 March 2020. Downloaded on 2/8/2026 12:45:32 PM. This article is licensed under a Creative Commons Attribution 3.0 Unported Licence.

Table 1 Water-splitting in biology and technology

	Catalysts	Electronic states	Generation of peroxide[a]
PSII	Mn_4CaO_5 only	Ground state (?)	None or ultrashort life-time
Artificial	Many variants	Photoexcited states	Generated

[a] Hydroperoxide is generally harmful to living bodies, while it can be a useful starting material in chemical syntheses.

We here summarize observations attained up to the binuclear Mn oxo complexes, which are relevant to the present study on Mn_4CaO_5.

(I) On charge separation (CS) dynamics, which should take place four times by four photon absorption to complete the circuit of a catalytic cycle: at each incident of CS, a proton and an electron are simultaneously lost from the moiety surrounding the possible catalyst, thereby keeping electric neutrality. The characteristics of CS dynamics to be noted are:

(I-A) CS dynamics generally passes across nonadiabatic regions (usually through conical intersections), inevitably accompanied by a nonadiabatic transition of adiabatic electronic states. The very basic mechanism of a single CS event is due to what we call coupled proton electron-wavepacket transfer (CPEWT), which is one of the so-called proton-coupled electron transfer (PCET) mechanisms.[23,24] In CPEWT, electron wavepackets and protons individually take different pathways (unlike hydrogen atomic migration) and arrive at different destinations in a single or multiple molecules, and thereby CS is realized in the acceptors.[17,18]

(I-B) Acceptors of electrons and protons for CPEWT can be different from each other and may be spatially separated so that electrons and protons are relay-transferred eventually to their final destinations. The Rydberg states of nitrogen atoms in amino acids, which usually form a highly quasidegenerate manifold of electronic states and spread broadly in space, often serve as a very good acceptor of transferred electrons.[19]

(I-C) CS due to CPEWT can take place not only in photoexcited states but even in ground electronic states. Ground-state charge separation is induced by collision (contact) with external molecules of positive charge. The quantum mechanism is similar to those of chemiluminescence or bioluminescence, and hence we refer to it as chemi-charge-separation.[20] CS in PSII is widely believed to take place in the electronic ground state, and this is yet hard to accept from the viewpoint of quantum dynamics. But this kind of dynamics has been clarified and justified by our study.[20]

(I-D) The Ca atom sitting close to the electron donating Mn has been found to dramatically prevent charge recombination between produced protons and electrons in CS.[18]

(II) Other elementary processes that are needed to materialize water-splitting catalytic cycles:

(II-A) Buffering of electrons and protons is necessary. For a catalytic cycle to be completed, electrons and protons that are lost (handed) to acceptors by CS dynamics should be recovered to their original positions. Hence electrons and protons to be supplied should be temporarily stored (or buffered) somewhere. For a mononuclear Mn oxo complex, molecules of such buffering functions are needed in addition to the oxo complex. Therefore the mono Mn oxo complex alone cannot work as a catalyst, even though it can perform CS. For a binuclear Mn oxo complex, it turns out that such external buffering molecules are not needed, since a part of the complex itself can work as a buffer.[21,22]

(II-B) Reloading (RL) of electrons and protons to the molecular center of CS is inevitable to resume the next CS dynamics.[22]

(II-C) Mn reduction (MR) is also needed. Due to the CS and/or RL processes, Mn atoms can become charge positive, and those positively charged Mn atoms should be neutralized (reduced) in order to continue the catalytic cycle.[22]

(II-D) Formation of O–O bonds: O–O bonds and/or O═O in the triplet state are to be formed.[21,22]

(II-E) Proton relay transfer along hydrogen-bonding water molecules is necessary.

(II-F) Radical chain transfer along hydrogen-bonding water molecules is also utilized.[21,22]

In terms of the above electron dynamics studies, we have thus found that a binuclear Mn oxo complex can serve as a catalyst for a four-photon photoexcited water-splitting cycle.

Here in this paper we construct a catalytic cycle in which a tetranuclear Mn oxo complex in the electronic ground state works as a catalyst without intermediate emergence of peroxides. The Mn complex we study is Mn_4CaO_5,[3] which is tied to acceptors of electrons and protons through hydrogen-bonded water molecules. Mn_4CaO_5 is schematically represented as $Mn^{(4)}$–O-Cub, where Cub indicates a skewed cubic structure composed of Mn_3CaO_4. We here set the following working hypotheses: (1) the mutual spatial orientation between the cluster and its adjacent acceptors of electrons and protons is basically maintained throughout the entire catalytic cycle, assuming that Mn_4CaO_5 does not rotate with respect to the surrounding molecular frame. We further assume that the terminal Mn (denoted as $Mn^{(4)}$) is solely responsible for all the four collision induced charge separations. (2) The skewed cubic part serves as a buffer of electrons and protons, and reloads three electrons and three protons that are lost in the first three CS dynamics. (3) After the final (fourth) CS dynamics is over, four protons and four electrons are extracted from water molecules leaving one oxygen molecule behind, and Mn_4CaO_5 is retrieved in the end.

The main aim of this paper is to examine whether the above hypotheses indeed work. Besides, attention is paid to the mechanism of reloading of protons and electrons to the appropriate places in the moiety of $Mn^{(4)}$, which should make it possible for the next CS from $Mn^{(4)}$ to resume. We also examine the role of Mn reduction processes to possibly generate an oxygen molecule and thereby complete one circuit of the catalytic cycle. To examine the entire scenario, we apply the method of nonadiabatic electron wavepacket dynamics and *ab initio* methodology for energetics.

Open Access Article. Published on 30 March 2020. Downloaded on 2/8/2026 12:45:32 PM.
This article is licensed under a Creative Commons Attribution 3.0 Unported Licence.

This paper first presents a series of model chemical schemes of an entire catalytic cycle in Section 2. Then the dynamics and energetics relevant to the water splitting are tracked numerically in Section 3. This paper concludes with Section 4 with some remarks.

2 Schematic representation of a catalytic cycle for water splitting by a tetranuclear Mn oxo complex

2.1 Molecular composition

2.1.1 Tetranuclear Mn oxo cluster to be studied. A model catalyst for the present water-splitting cycle is shown in Fig. 1 with labels for some characteristic atoms. An atom X labeled with *i* is referred to as $X^{(i)}$. The core of the model catalyst is a tetranuclear Mn oxo complex represented as $Mn_4Ca(OH)_5(HCOO)_5(H_2O)_4$ or a little more precisely $Mn_3Ca(H_2O)_2(OH)_4(HCOO)_5$–OH–$Mn(H_2O)_2$. Mn at the terminal position, customarily referred to as $Mn^{(4)}$, is coordinated by two water molecules. Likewise, two H_2O are bonded to the Ca atom, which is supposed to play a key role as a proton source and as a member to participate in the formation of an oxygen molecule. The skewed cubic $Mn_3Ca(H_2O)_2(OH)_4$ cluster is coordinated by five carboxy (HCOO) groups as shown in Fig. 1b. Three of the HCOO groups bridge $Mn^{(1)}$–$Mn^{(2)}$, $Mn^{(2)}$–$Mn^{(3)}$, and $Mn^{(3)}$–$Mn^{(1)}$ in a symmetric manner, but two of the HCOO bridge $Mn^{(1)}$–Ca and $Mn^{(2)}$–Ca, but not $Mn^{(3)}$–Ca. $Mn^{(3)}$ is chemically bonded to $Mn^{(4)}$ through OH.

As a result, the Mn_4CaO_5 cluster has a rather large open space, which is roughly surrounded by $Mn^{(4)}$, $O^{(4)}$, $Mn^{(3)}$, $O^{(2)}$, $O^{(5)}$, and Ca. We refer to this open-space as the reaction field for water splitting. Indeed one can see such an open space in the crystal structure of Mn_4CaO_5 in Fig. 2 of ref. 2. This open space can be used also for in-and-out motion of molecules such as external water molecules and oxygen molecules. We place two water molecules marked with $O^{(6)}$ and $O^{(7)}$ in the reaction field as depicted in Fig. 2. These molecules can serve as a hydrogen-bonding network to relay-transport protons by connecting the skewed cubic Mn_3Ca oxo complex and $Mn^{(4)}(H_2O)_2$. Also, these water molecules are involved in the reloading of protons as a part of an H-bond network and are supposed to play a role in oxygen generation. Other important chemical dynamics can take place in this space. By contrast, the other sides of the cubic structure of $Mn_3Ca(H_2O)_2$ are shielded by the carboxy groups, and it is rather hard to approach $Mn^{(1)}$, $Mn^{(2)}$, $O^{(1)}$ and $O^{(2)}$.

The present work assumes that all the bridging oxygen atoms in the skewed cubic structure Mn_3CaO_4 of the S_0 state in the Kok cycle (here K_0 of Fig. 2), the bridge being termed as a μ-oxo bridge, are all hydroxylated as –OH–. Among the others, however, only two hydroxyl groups, $O^{(2)}H$ and $O^{(5)}H$, are essential for the present water-splitting dynamics, since only these two groups face the reaction field.

It does not seem easy for X-ray related experiments to determine whether the μ-oxo bridge is hydroxylated, since the hydrogen atoms in this circumstance are too small.[3,6] However, it is natural to presuppose the presence of hydroxy groups under the circumstance where the Cl^- ions exist nearby the cluster.[2] In fact, Landman *et al.*[9,25] have experimentally discussed the presence of a μ-hydroxo bridge even in gas phase Mn oxo clusters such as $Ca_nMn_{4-n}O_4{}^+$. Mafune and his group have also identified the presence of a μ-hydroxo bridge in the Mn_4CaO_5 cluster with vibrational spectroscopy, the hydroxy groups having been formed by collision of the naked Mn_4CaO_5 with water molecules in the gas phase.[26] Furthermore, Lohmiller *et al.* have explicitly evidenced the presence of a μ-hydroxo bridge at least for $O^{(5)}$ in Mn_4CaO_5 taken from native PSII.[27] In our proposed model, the relative positions of $O^{(2)}$ and $O^{(5)}$ are mutually symmetric, and hence we also assume the bridge of $O^{(2)}$ to be hydroxylated. Later, those protons on $O^{(2)}$ and $O^{(5)}$ will be shown to originate from water molecules that are split in the catalytic cycle. We assume that $O^{(1)}$, $O^{(3)}$ and $O^{(4)}$ are also hydroxylated, but these protons will turn out not to be directly involved in water oxidation.

The Mn_4Ca oxo complex serves as an electron–proton donor (EPD), the formal oxidation state of which is represented as H_3–EPD–H. Here H_3 on the left side are located on the cubic structure Mn_3CaO_4, whereas H on the right side is one of H atoms in the water molecule coordinated to $Mn^{(4)}$, see panel K_0 in Fig. 2. Note that the three hydrogens on the left-hand-side of H_3–EPD–H are located at $O^{(2)}$ and $O^{(5)}$ and in one of the H_2O on the Ca atom.

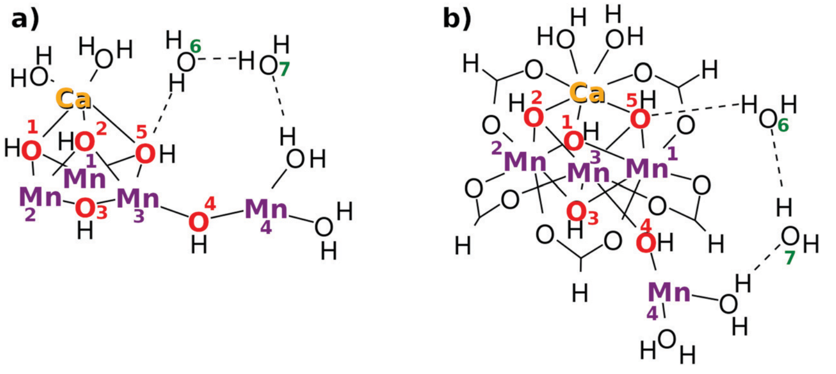

Fig. 1 Composition of the Mn_4Ca oxo complex with two hydrogen-bonded water molecules. Panel (a) shows an abbreviated graphical representation for simpler visualization. (b) In our treated full system, five carboxy groups bridge either Mn–Mn or Mn–Ca. In the text, the shorthand expression (a) is often used for representing the chemical scheme, but the expression (b) is actually adopted in the numerical studies.

Open Access Article. Published on 30 March 2020. Downloaded on 2/8/2026 12:45:32 PM.
This article is licensed under a Creative Commons Attribution 3.0 Unported Licence.

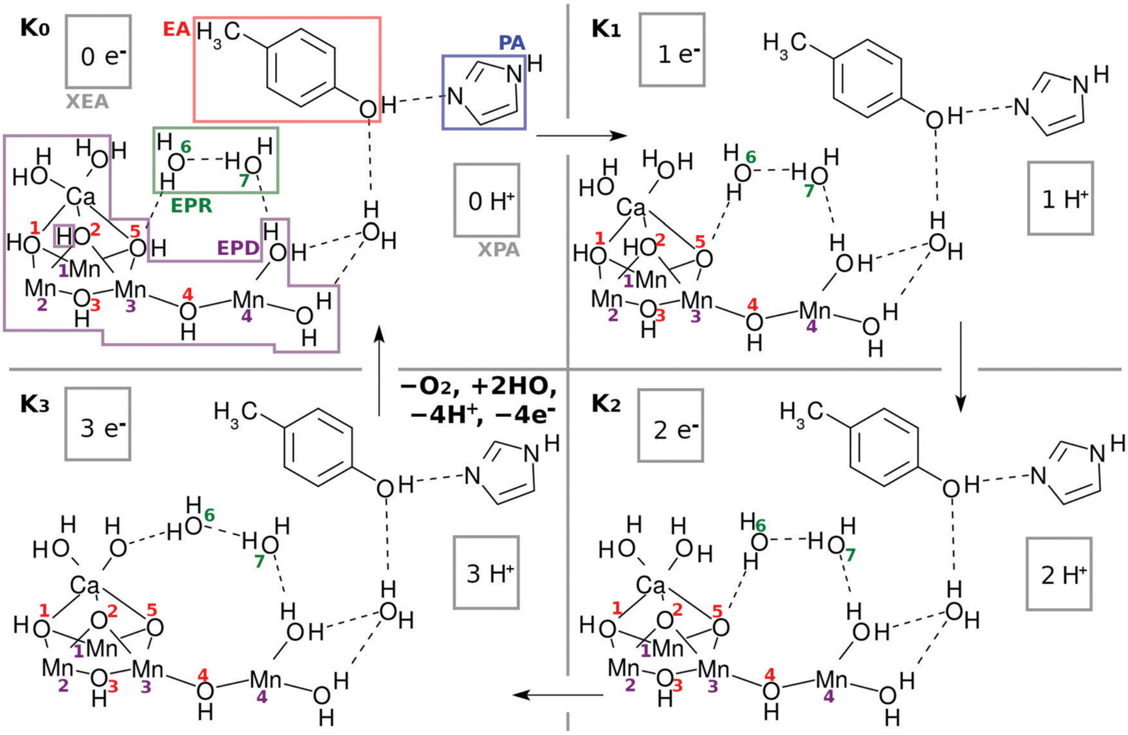

Fig. 2 Chemical scheme of the K-state cycle of water-splitting catalyzed by the Mn_4Ca oxo complex. See the text for the labeling scheme. Note that the five carboxy groups bridging either Mn–Mn or Mn–Ca in EPD are not shown here. See Fig. 1b to find the full expression. The H of H_3 in H_3–EPD–H is on either $O^{(2)}$, $O^{(5)}$, or Ca–OH, while H on the right hand side of H_3–EPD–H lies on $Mn^{(4)}$–OH. Note that H on $O^{(2)}$ is not a member of the definition of EPD in K_0.

The 3 + 1 structure, that is, the oxo complex composed of Mn_3Ca and the terminal $Mn^{(4)}$, naturally suggests a hypothesis that only $Mn^{(4)}$ is responsible for the charge separation. The molecular orbital (MO) of $Mn^{(4)}$ from which an electron is abstracted should be high enough in energy and diffuse enough in space to access an electron acceptor. This feature is brought about by keeping $Mn^{(4)}$ coordinated by less anionic ligands. This is the "1" part of the 3 + 1 structure. On the other hand, water oxidation needs low energy and vacant MOs to abstract an electron from a water molecule in the end. This feature is realized by placing many anionic ligands on Mn atoms in the "3" part of the 3 + 1 structure. The view of the 3 + 1 structure, $Mn_3CaO_4(H_2O)_2$ as the "3" part and $MnO(H_2O)_2$ as the "1" part, is in harmony with the widely accepted structure of the natural oxygen-evolving complex in PSII.[1–3,6–8]

2.1.2 Composition of a catalytic system to yield electrons and protons. The components to be adopted in an entire water-splitting system are listed as follows, see panel K_0 of Fig. 2 for the corresponding graphical representations. The molecules after the colon in each item below show the biological correspondence in PSII:[28]

- an electron–proton donor (H_3–EPD–H): oxygen-evolving complex (OEC) including the Mn_4CaO_5 cluster
- an electron acceptor (EA–H = 4-methylphenol): D1-Y161 or TyrZ (Y_Z)
- a proton acceptor (PA–H = imidazole): D1-H190 or HisZ
- electron–proton resources and a bridging water molecule between EPD and EA (EPR = $2H_2O$): water cluster between OEC and TyrZ
- an external electron acceptor (XEA): P680
- an external proton acceptor (XPA): lumenal bulk phase

Here again H_3–EPD–H = $Mn_4Ca(OH)_5(H_2O)_4(HCOO)_5$ (see Fig. 1).

The pair of electron acceptor EA and proton acceptor H–PA is a Y-shaped acceptor consisting of intramolecularly polarized 4-aminophenol and imidazole.[19] The electron and the proton thus drawn apart on this Y-shaped acceptor are assumed to be further transported through their own pathways to XEA and XPA, respectively.

The external electron acceptor XEA finally accepts those isolated electrons. The external proton acceptor XPA has the same role for protons. In the present study, the functions of XEA and XPA are not defined explicitly,[21] and they will be implicitly addressed only in the study of energetics.

2.2 Overview of the catalytic cycle proposed

2.2.1 Collision induced charge separation (chemi-charge-separation). It is widely believed that charge separation by the Mn_4CaO_5 cluster is performed without direct photoabsorption. This phenomenon is as puzzling as ground state molecules emitting light. The driving force of this dynamics is often (intuitively) accounted for in terms of the ladder sequence of the oxidation–reduction potential, which is supposed to be initiated by photoabsorption somewhere away from Mn_4CaO_5. However, such an explanation is never obvious from the viewpoint of quantum mechanics, since inter-molecular electron transfer accompanied by proton transfer is a typical phenomenon

Open Access Article. Published on 30 March 2020. Downloaded on 2/8/2026 12:45:32 PM. This article is licensed under a Creative Commons Attribution 3.0 Unported Licence.

of "excited-state proton transfer" due to the passage of a nonadiabatic transition.[29] However, this puzzle has been resolved by our nonadiabatic electron wavepacket study:[20] as in chemiluminescence or bioluminescence, reactant molecules prepared initially in their electronic ground-states are led to undergo a nonadiabatic transition in the course of reaction, the counterpart potential energy surface of which comes down to cross the ground state potential, making a conical intersection.[30] Thus an electronic-ground state can undergo a nonadiabatic transition being induced by collision. We refer to this phenomenon as chemi-charge-separation. In the present study of the charge separation dynamics of Mn_4CaO_5, we also suppose that this mechanism works four times.

Fig. 3 and its caption show an example of the mechanism of chemi-charge-separation in the case of the mononuclear Mn oxo complex: (1) an outer molecule denoted as EA0, which has been oxidized somewhere else originally due to photoabsorption, approaches to make contact with EA, which induces CPEWT from EA – synchronous transfer of an electron wavepacket to EA0 and of a proton to PA. After EA0 captures the electron, it leaves the stage and the coherent overlap between the two electronic states of EA0 and EA is switched off, shutting off the channel of time-reversal of the reaction. (2) Then another ground-state nonadiabatic dynamics follows, where an electron wavepacket jumps from EPD (a Mn oxide) to EA, along with the return (thus making a reciprocal motion) of a proton from PA to EA.[31] (3) Then proton relay-transfer occurs from EPD to PA, leaving electronic polarization in EPD. (4) PA captures a proton, while EA0 adopts an electron, and thereby charge separation is completed. It turned out incidentally that the reciprocal motion of a proton between EA and PA plays a crucial role to maintain the electric neutrality of EPD and EA and furthermore this type of motion is physically relevant to one-way (non-reversible) transfer of electrons.[31]

In what follows, our dynamical calculations presented in Fig. 2 begin with stage (2) of Fig. 3 after the electron transfer due to the contact of EA0 and EA has been successfully finished.

2.2.2 Conditions for efficient charge separation. For the collision-induced charge separation to be efficiently performed, the overlap of electronic wavefunctions between EPD and EA should be as large as possible. In this aspect, the relative molecular orientation of them as schematically represented in K_0 (left-top panel) of Fig. 2 seems acceptable, where $Mn^{(4)}$ is nearest to the EA part. Indeed it turns out that an electron sitting in a 4s-like spatially diffuse state of $Mn^{(4)}$ is involved in such electron wavepacket transfer to EA. The cubic structure of $Mn_3CaO_4(H_2O)_2$ of the cluster is covered by carboxy groups to maintain its structure, which is inconvenient for transfer of electrons or protons. Besides, to the best of our knowledge, there is no report that actually has detected the reorientation motion of the Mn_4CaO_5 cluster with respect to the position of EA. On the contrary, it is reported that one of the water molecules coordinated to the Ca atom has a hydrogen-bond (directly or indirectly) with the TyrZ molecule,[2] thus suggesting that the relative position and orientation of the skewed cubic structure of $Mn_3CaO_4(H_2O)_2$ are at least loosely fixed in space.

Under this situation, it is quite natural to assume that $Mn^{(4)}$ alone must be responsible for all the four charge-separation dynamics, that is, electrons and protons should be provided to

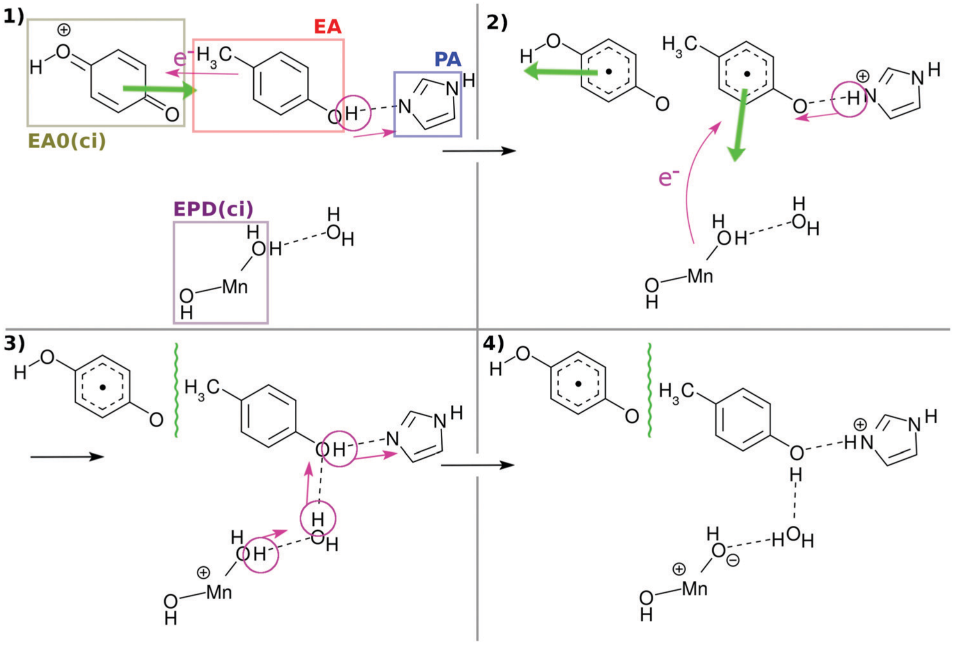

Fig. 3 Schematic illustration of the mechanism of collision-induced (ci) charge separation catalyzed by the mononuclear Mn oxo complex.[20] All the charge separations in the present tetranuclear system proceed in qualitatively the same manner as this scheme. The green thick arrow denotes the translation of the molecules to approach or to recede. EA0(ci) and EPD(ci) denote the primary electron acceptor and electron–proton donor for the collision-induced mechanism, which correspond to XEA and EPD in the present mechanism, respectively. The wavy line between EA0(ci) and EA indicates that there is a long distance between them for quantum coherence to be broken.

Open Access Article. Published on 30 March 2020. Downloaded on 2/8/2026 12:45:32 PM.
This article is licensed under a Creative Commons Attribution 3.0 Unported Licence.

EA and PA, respectively, only through the close surroundings of $Mn^{(4)}$. Indeed, we will show that this can be the case if the electronic and protonic states of this area can be well restored on each occasion of charge separation. Such recovery will be assisted by reloading of electrons and protons from the site of the skewed cubic structure $Mn_3CaO_4(H_2O)_2$ and eventually from external water molecules such as those in EPR of Fig. 2.

2.2.3 Model catalytic cycle of four K-state nodes. On the basis of the above presupposed conditions, we propose a model of a catalytic cycle of ground-state water splitting in terms of Mn_4CaO_5 of Fig. 1. Fig. 2 schematically shows the global structure of the model, which we refer to as the K-state cycle after the Kok-cycle (also referred to as the S-cycle). It consists of four charge separation dynamics, each state of which is denoted as K_n (K_0, K_1, K_2, and K_3). Each charge separation further drives an individual sequence of chemical processes, which are in turn denoted as $K_{nm} \rightarrow K_{n(m+1)}$ (*e.g.*, $K_{14} \rightarrow K_{15}$) as discussed in the sequence of figures from Fig. 4–11. K_4 is of course equivalent to K_0 after a complete circuit of the cycle.

The structures of all the K_{nm} states schematically represented in the figures have been actually confirmed to be sitting in their local minima of the ground-state potential energy surfaces. Hence the molecular states appearing here are realistic in this sense.

The K-state representation is analogous to the Kok cycle of PSII.[7] A major dissimilarity is that the K-cycle has only 4 nodes, rather than 5 in the Kok cycle, since we treat the S_4 state as an intermediate state appearing between the K_3 and K_0 state.

The present model catalytic cycle has been designed under the understanding that the stable and robust charge separation dynamics is the most vital process for water splitting in nature. Then the other chemical machineries, such as reloading of electrons and protons and the reduction of $Mn^{(4)}$, will rather automatically follow to assist the completion of the four step charge separation.

2.3 Working catalytic system in the precise scheme of the K-state cycle

We next describe how the transitions in K-states work. Note beforehand that the elementary subprocesses K_{nm} are consecutive members of K_n, although we describe each below as though it represents a single event. For example, some reactions involving proton relay-transfer (*e.g.*, $K_0 \rightarrow K_{01}$ and $K_{04} \rightarrow K_{05}$) are regarded as a single process, even if local minima exist along the reaction paths.

In transitions from the K_0 state to K_1, K_1 to K_2, and K_2 to K_3, the processes include only charge separation (CS) and reloading (RL). Only in the last transition from K_3 to K_0 do we discuss, besides CS, the final reduction of the $Mn^{(4)}$ atom, water molecule decomposition, and associated O_2 formation. The details of the individual subprocesses are described in the figure captions so that the events can be tracked only by watching the figures.

2.3.1 Transition from the K_0 state; CS and RL. The catalytic cycle begins with charge separation as K_0 in Fig. 4. This figure illustrates a sequence of reactions up to a stage in which an electron and a proton are given away to XEA and XPA. Note that an electron is already handed to XEA before the panel of K_0 begins, but EA0 (see Fig. 3) is consistently omitted in the following figures.

As a result of donation of an electron and a proton, $Mn^{(4)}$ and the OH site next to it become electronically polarized.

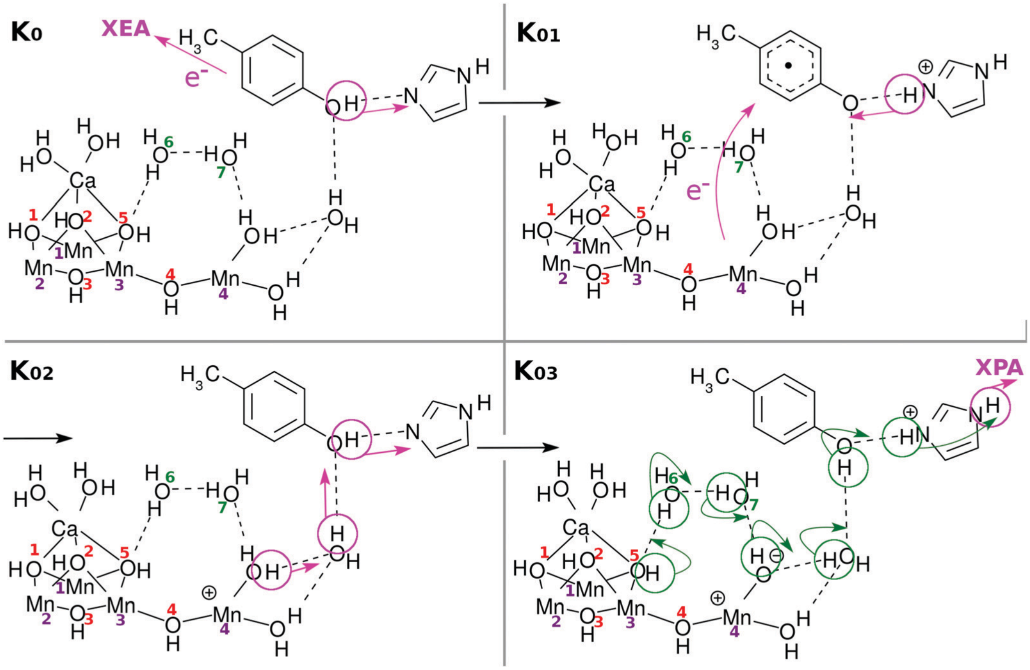

Fig. 4 Chemical scheme of the first charge separation (CS(1)). An electron transfers from EA to XEA, coupled to the proton transfer from EA to PA ($K_0 \rightarrow K_{01}$). Then an electron transfers from EPD to EA, being coupled to the proton transfer back from PA to PA ($K_{01} \rightarrow K_{02}$: CS(1)). These two mechanisms are both collision-induced CPEWT. When EA approaches EPD close enough, a ground-state proton relay-transfer occurs ($K_{02} \rightarrow K_{03}$). Proton transfer from PA to XPA is coupled to H-bond reorganization ($K_{03} \rightarrow K_{04}$).

Open Access Article. Published on 30 March 2020. Downloaded on 2/8/2026 12:45:32 PM.
This article is licensed under a Creative Commons Attribution 3.0 Unported Licence.

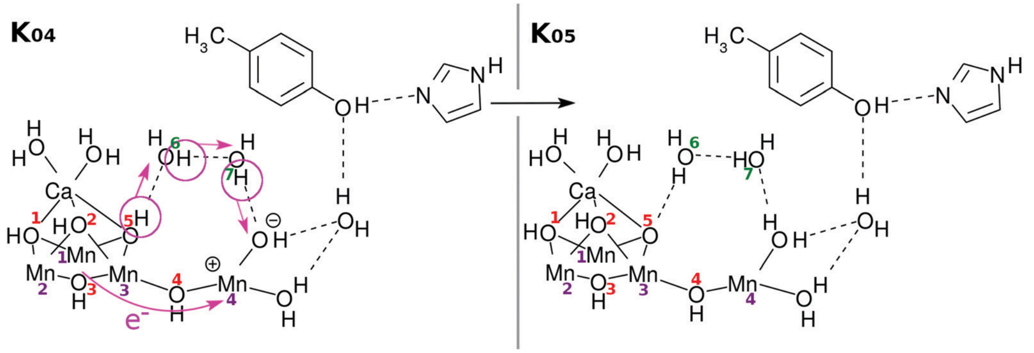

Fig. 5 Chemical scheme of the first reloading (RL(1)). Intramolecular electron transfer from the Mn_3Ca part (the "3" part) to the $Mn(OH_2)_2$ part (the "1" part) ($K_{04} \rightarrow K_{05}$: RL(1)). Here a proton relay-transfer begins from $O^{(5)}H$. The state of K_{05} is schematically equal to K_1.

For the next charge separation dynamics to resume, the vacancy in the 4s-like diffuse orbital on $Mn^{(4)+}$ needs to be refilled, and also a proton should be reloaded to the right position.

Fig. 5 suggests one of such possible reloading processes: the panel for the state K_{04} suggests that an electron transfers from the skewed cubic structure to $Mn^{(4)+}$, while a proton is relay-transported from $O^{(5)}$. The electric neutrality is thus maintained, although the radical property can be significantly changed.

Incidentally we note that the transition from K_0 to K_{05}, which is essentially equal to K_1, can take place in dark conditions, as long as some EA0 molecules happen to remain in the molecular system. The possible collision of such active EA0 with EA will bring the K_0 state to K_1, the reverse reaction of which cannot happen, whereas the K_1 state cannot proceed to K_2 because of the lack of active EA0 in the dark place. In this regard it has been found that S_1 is automatically produced from S_0 due to oxidation by D2-Tyr160 even in dark conditions.[7]

2.3.2 Transition from the K_1 state; CS and RL. In the next stage of collision-induced charge separation, similar dynamics is repeated with respect to $Mn^{(4)}$ and its vicinity, see the four panels in Fig. 6. $Mn^{(4)}$ gives up an electron sitting until then in the diffuse 4s-like orbital, and a proton is carried through the network in EPR. It is noticed that only one of either $H_2O^{(6)}$ or $H_2O^{(7)}$ suffices to work as a member of the proton-relay network. This is also the case for other transitions from K_1 and K_2.

Here again the reloading process is needed for the next charge separation dynamics to materialize. There can be multiple ways of reloading, and we show only one of the likely channels in Fig. 7.

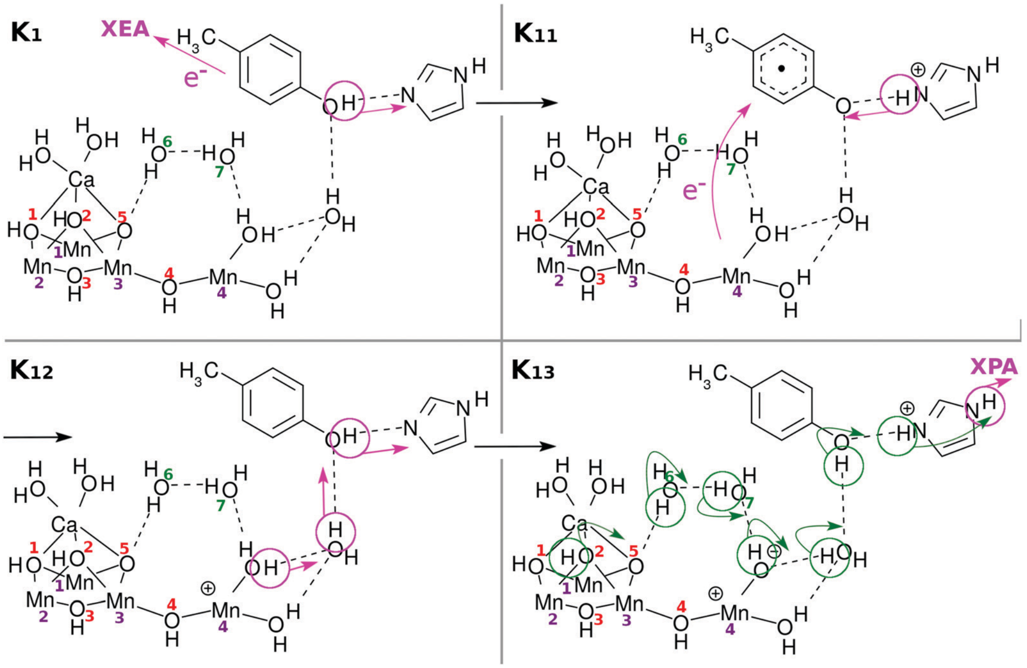

Fig. 6 Chemical scheme of the second charge separation (CS(2)). An electron transfers from EA to XEA, coupled to the proton transfer from EA to PA ($K_1 \rightarrow K_{11}$). Then an electron transfers from EPD to EA, being coupled to the proton transfer back from PA to EA ($K_{11} \rightarrow K_{12}$: CS(2)). These two mechanisms are both collision-induced CPEWT. When EA approaches EPD more closely, ground-state proton relay-transfer occurs ($K_{12} \rightarrow K_{13}$). Proton transfer from PA to XPA is coupled to H-bond reorganization ($K_{13} \rightarrow K_{14}$).

Open Access Article. Published on 30 March 2020. Downloaded on 2/8/2026 12:45:32 PM.
This article is licensed under a Creative Commons Attribution 3.0 Unported Licence.

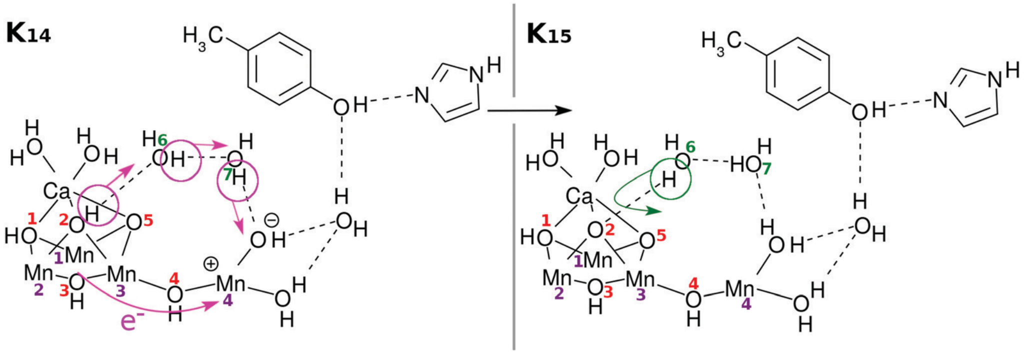

Fig. 7 Chemical scheme of the second reloading (RL(2)). Intramolecular electron transfer from the Mn_3Ca part (the "3" part) to the $Mn(H_2O)_2$ part (the "1" part) of the Mn_4Ca oxo complex with the "3 + 1" structure ($K_{14} \rightarrow K_{15}$: RL(2)). A proton relay-transfer occurs from $O^{(2)}H$. Hydrogen-bond reorganization gives K_2.

Once again an electron is transferred from the skewed cubic structure and a proton is abstracted from the site of $O^{(2)}H$. The positions of $O^{(2)}H$ and $O^{(5)}H$ are mutually symmetric and there is no reason to distinguish them at this stage.

Incidentally, it is demonstrated in the Kok cycle that only an electron is released in the transition from S_1 to S_2.[6,7] This does not seem to be consistent with our model of the transition from K_1 to K_2, in which both an electron and a proton are handed over to the acceptors due to the charge separation dynamics. However, a direct comparison between experiments and the present theoretical results is not rationalized, since in contrast to our simple theoretical calculations, the experimental observations of protons and electrons are made indirectly through complicated channels of proteins and such.

2.3.3 Transition from the K_2 state; CS and RL.

The third charge separation dynamics follows in Fig. 8. Except for minor details, nothing essentially new is added in this process.

Again an electron is reloaded from the cubic subcluster. However, we see a new feature in the reloading process as shown in Fig. 9. Since $O^{(1)}H$ and $O^{(3)}H$ lie on the opposite side of the reaction field, the protons attached to them are hard to dispatch. Instead it is likely that one of the protons of the water molecules coordinated to Ca atom will be removed and relay-transferred (see K_{25} in Fig. 9). Thus, finally three electrons and three protons are subtracted from the skewed cubic structure $Mn_3CaO_4(H_2O)_2$.

2.3.4 Transition from the K_3 state back to K_0; CS and O_2-formation.

Then the final (fourth) charge separation dynamics

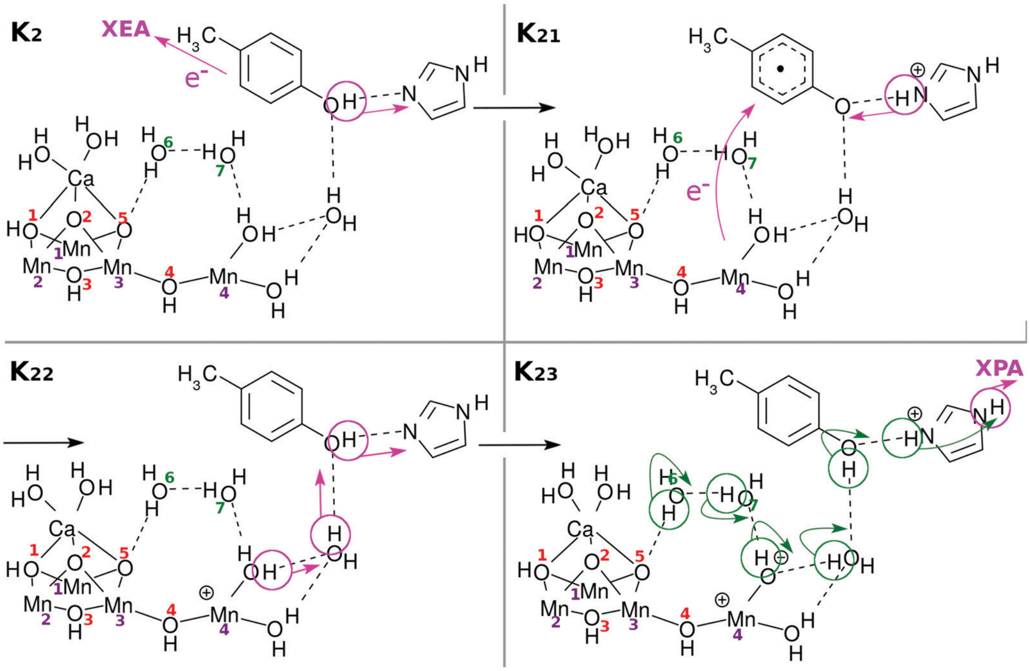

Fig. 8 Chemical scheme of the third charge separation (CS(3)). An electron transfers from EA to XEA, coupled to the proton transfer from EA to PA ($K_2 \rightarrow K_{21}$). Then an electron transfers from EPD to EA, being coupled to the proton transfer back from PA to EA ($K_{21} \rightarrow K_{22}$: CS(3)). These two mechanisms are both collision-induced CPEWT. When EA approaches closer to EPD, a ground-state proton relay-transfer occurs ($K_{22} \rightarrow K_{23}$). The proton transfer from PA to XPA is coupled with H-bond reorganization ($K_{23} \rightarrow K_{24}$).

Open Access Article. Published on 30 March 2020. Downloaded on 2/8/2026 12:45:32 PM.
This article is licensed under a Creative Commons Attribution 3.0 Unported Licence.

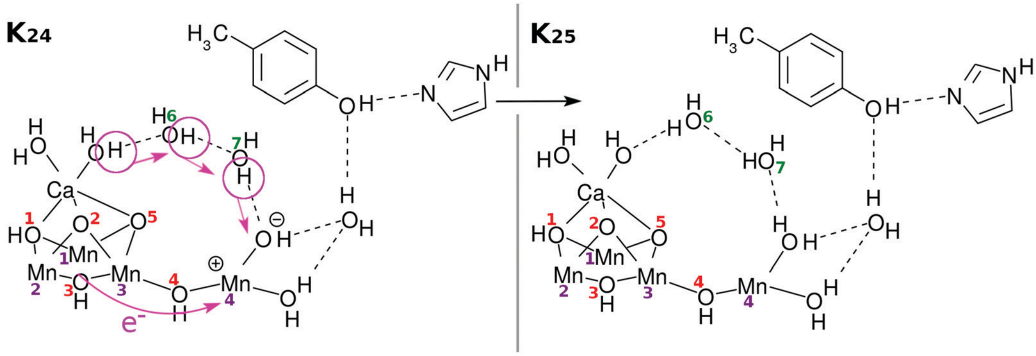

Fig. 9 Chemical scheme of the third reloading (RL(3)). Intramolecular electron transfer from the Mn_3Ca part (the "3" part) to the $Mn(H_2O)_2$ part (the "1" part) ($K_{24} \rightarrow K_{25}$: RL(3)). This time a proton transfer begins from $CaOH_2$. Hydrogen-bond reorganization gives K_3.

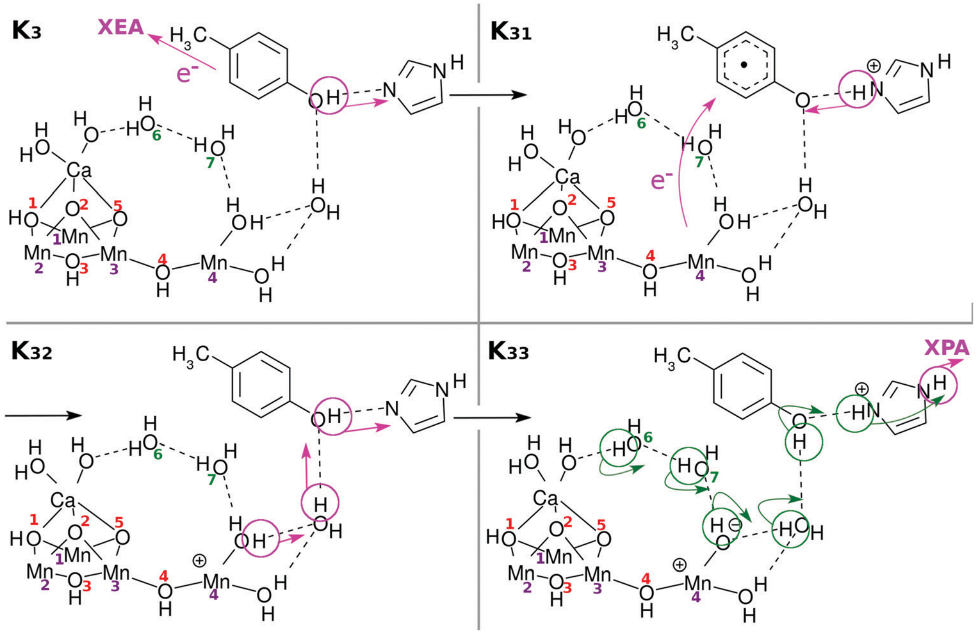

Fig. 10 Chemical scheme of the fourth charge separation (CS(4)). An electron transfers from EA to XEA, coupled to the proton transfer from EA to PA ($K_3 \rightarrow K_{31}$). Then an electron transfers from EPD to EA, being coupled to the proton transfer back from PA to EA ($K_{31} \rightarrow K_{32}$: CS(4)). These two mechanisms are both collision-induced CPEWT. When EA approaches closer to EPD, a ground-state proton relay-transfer occurs ($K_{32} \rightarrow K_{33}$). Proton transfer from PA to XPA is coupled with H-bond reorganization ($K_{33} \rightarrow K_{34}$).

resumes before completing the catalytic cycle as shown in Fig. 10. Nothing particularly new is expected in this CS. However, an essentially different process than those of the simple reloading dynamics up to the K_3 state is anticipated at this stage, since the cluster becomes ready to extract four electrons and four protons from two water molecules, leaving an oxygen molecule simultaneously.

There have been many mechanisms proposed about oxygen generation catalyzed by Mn_4CaO_5 in PSII, aside from those in the studies of artificial photocatalytic reactions. Siegbahn opened this field of quantum chemistry, to the best of our knowledge, and has been leading since then[1,32–34] (see also ref. 8, 35, 36 and references cited therein). We here propose another possible mechanism as illustrated in Fig. 11: first the above Ca–OH reduction is coupled with simultaneous (concerted) formation of an $O^{(5)}$–$O^{(6)}$ bond ($K_{34} \rightarrow K_{35}$). Then a proton is transferred from $O^{(5)}$–$O^{(6)}$ to $Mn^{(4)}$–OH ($K_{35} \rightarrow K_{36}$). Also synchronous electron transfer from $O^{(5)}$–$O^{(6)}$ leads to the release of molecular oxygen O_2. This reaction may also be coupled to $K_{36} \rightarrow K_{37}$. The resultant vacancy produced by the O_2 release is filled by the H_2O on the Ca atom, and $H_2O^{(7)}$ is attached on Ca ($K_{36} \rightarrow K_{37}$). Proton transfer to $O^{(2)}$ from one of the three H_2O molecules is coupled with $Mn^{(1)}$–O, $Mn^{(3)}$, and Ca–O bond formation. To fully reproduce K_0, two H_2O molecules need to be supplied from the environment ($K_{37} \rightarrow K_0$). In this particular mechanism of O_2 generation, an oxygen atom ($O^{(5)}$ in this figure or $O^{(2)}$ as well) at one of the μ-hydroxo bridges is exchanged (replaced) with an oxygen of some of the water molecules. Also, one of the water molecules initially attached to Ca atom is likely to be replaced with another H_2O after all the cycle is completed. We refer to ref. 4, 5, 36 and 37 for the extensive

Open Access Article. Published on 30 March 2020. Downloaded on 2/8/2026 12:45:32 PM. This article is licensed under a Creative Commons Attribution 3.0 Unported Licence.

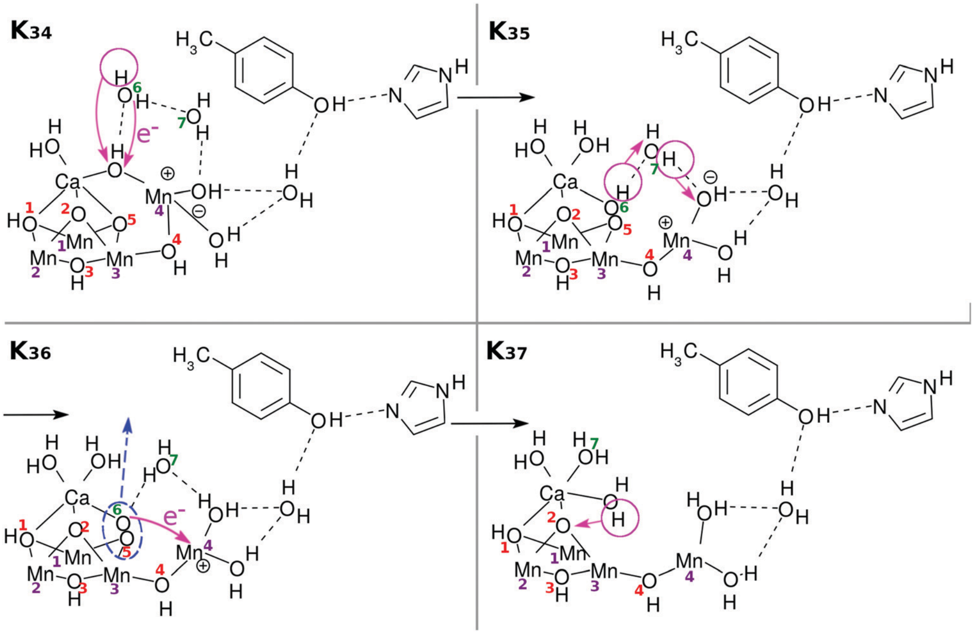

Fig. 11 One of the possible chemical schemes of Mn reduction. Ca–OH reduction is coupled to $O^{(5)}$–$O^{(6)}$ bond formation ($K_{34} \rightarrow K_{35}$). A proton is transferred from $O^{(5)}$–$O^{(6)}$ to $Mn^{(4)}$–OH ($K_{35} \rightarrow K_{36}$). An electron transfers from $O^{(5)}$–$O^{(6)}$, being coupled to the release of molecular oxygen O_2. This reaction may also be coupled to the process of $K_{36} \rightarrow K_{37}$. The resultant vacancy given by the O_2 released is filled by a H_2O on the Ca atom, and $H_2O^{(7)}$ is attached on Ca ($K_{36} \rightarrow K_{37}$). Proton transfer from one of the three H_2O molecules to $O^{(2)}$ is coupled to $Mn^{(1)}$–O, $Mn^{(3)}$, and Ca–O bond formation. This completes one cycle of the present water splitting. To make a full reproduction of K_0, two external H_2O molecules need to be supplied from the environment ($K_{37} \rightarrow K_0$).

discussion of the possible replacement of those oxygen atoms. This completes one cycle of the present water splitting.

An important note with respect to Fig. 11 is that we intentionally do not draw the two water molecules to be inserted to bring the stage of K_{37} back to K_0, just for clearer graphical illustration. The series of schemes from K_0 to K_{37} is self-contained in that water splitting is achieved within the molecular system initially prepared in K_0 and that two water molecules are added after or during the process up to K_{37}. However, it is obvious that additional water molecules invited from outside should work so as to help the system proceed favorably. For instance the oxygen molecule generation depicted in K_{36} in Fig. 11 should take place in a concerted manner with the water insertion, which should suppress the energy required to form O_2.

Note that the reloading processes are not necessarily unique and may have multiple reaction pathways, the flexibility brought about by which should give robustness to plants in nature. Accordingly, there can exist other mechanisms of O_2 generation, depending on the reloading processes realized up to the state K_3. For instance, external water molecule(s) can be introduced even at a stage as early as when the subprocess K_{15} finishes, where two protons have been removed from $O^{(2)}$ and $O^{(5)}$ (not demonstrated graphically). Such insertion of an additional water molecule can give rise to a different mechanism of O_2 generation. Likewise, O_2 may be given through other multiple paths with different probability weights. It is also likely that different experimental observations may emphasize different mechanisms. We do not get involved in further exploration of new possible mechanisms of O_2 generation in this paper.

3 Dynamics and energetics behind the proposed mechanism

The proposed model of the catalytic cycle has been built up not only based on the knowledge learned from the literature but in terms of our own theoretical and computational studies. We here in this section show such theoretical and computational background that has led us to a picture of water splitting.

We first note that we could not perform the full dimensional nonadiabatic electron wavepacket dynamics calculations over the entire system, from those of K_0 to K_3 in Fig. 2. This is simply because the entire system is far larger than our computational capability. The largest obstacle is that we have four Mn atoms that together make exceedingly huge active spaces in which to sufficiently describe the relevant open-shell electronic states. So our strategy is to perform nonadiabatic electron wavepacket dynamics in terms of state-averaged SA-MCSCF type electronic wavefunctions for the four charge separation dynamics through the $Mn^{(4)}$ atom only. Since it is key to the present study to assure that such four-step charge separation through $Mn^{(4)}$ is indeed possible, we need to achieve rather faithful nonadiabatic electron wavepacket calculations to track the real-time CPEWT dynamics. In these calculations, the active spaces relevant to the other Mn atoms ($Mn^{(1)}$ to $Mn^{(3)}$) are fixed. In addition, we could not help omitting the Ca atom and its attached groups from the skewed cubic structure, namely, $Ca(H_2O)_2$ $(HCOO)_2$ again, for the reason of computational limitation.

Then each of the four charge separations is followed by individual reloading dynamics. For the same computational

Open Access Article. Published on 30 March 2020. Downloaded on 2/8/2026 12:45:32 PM. This article is licensed under a Creative Commons Attribution 3.0 Unported Licence.

limitation reason as above, we apply a modified unrestricted Hartree–Fock (UHF) method to track nonadiabatic nuclear paths in an analogous manner to the *ab initio* MD method. With these simplified calculations we reach the conclusion that electrons are certainly transported from the skewed cubic structure of $Mn_3CaO_4(H_2O)_2$ to reload the 4s-like diffuse orbital of $Mn^{(4)}$.

The energy profile of the entire reaction scheme and some other structural calculations as well will be illustrated in terms of *ab initio* configuration interaction calculations. Note that none of the numerical calculations here is aimed at high accuracy performance but qualitative pictures and notions are the goal of this work.

Incidentally, no solvent effect has been taken into account except for the hydrogen-bonded water clusters. Nor are included the protein fields that are supposed to physically support the catalytic system. In these senses the present work is still far from the level of a simulation study.

3.1 Computational methodology

Below we describe the methodological details mainly for the dynamics computations. (See Section S1 of the ESI† for the details of energetics.[65])

3.1.1 Theory of nonadiabatic electron wavepacket dynamics. Since the main focus of our numerical study is on the series of charge separation dynamics, we need a method of nonadiabatic electron wavepacket study. One of the systematic methods to treat such electron dynamics is the path-branching representation theory,[38–41] in which quantum electron wavepackets propagate in time along branching nuclear paths. It is briefly outlined as follows.[40,41]

First, the electron wavepacket $\Psi_{\text{elec}}(\mathbf{r},t;\mathbf{R}(t))$ is expanded in a set of time-independent wavefunctions $\{\Phi_I(\mathbf{r};\mathbf{R})\}$ at each nuclear configuration $\mathbf{R}$ as

$$\Phi_{\text{elec}}(\mathbf{r},t;\mathbf{R}(t)) = \sum_I C_I(t)\Phi_I(\mathbf{r};\mathbf{R})|_{\mathbf{R}=\mathbf{R}(t)}, \qquad (2)$$

with $C_I(t)$ being the Ith time-dependent coefficient to be evaluated at each time step. The vector $\mathbf{r}$ denotes the collective representation of all electrons. The time-variation of $\mathbf{R}$ makes a nonclassical nuclear path $\mathbf{R}(t)$ that carries the electronic wavefunction at time t. Then the coupled equations of motion for the electron wavepackets are given as

$$\begin{aligned} i\hbar\frac{\mathrm{d}C_I}{\mathrm{d}t} &= \sum_J \Big[H_{IJ}^{(\text{el})} - i\hbar\sum_k \dot{R}_k X_{IJ}^k \\ &\quad - \frac{\hbar^2}{4}\sum_k (Y_{IJ}^k + Y_{JI}^{k*})\Big] C_J, \end{aligned} \qquad (3)$$

where

$$\begin{aligned} H_{IJ}^{(\text{el})} &= \left\langle \Phi_I \middle| \hat{H}^{(\text{el})} \middle| \Phi_J \right\rangle, \\ X_{IJ}^k &= \left\langle \Phi_I \middle| \frac{\partial}{\partial R_k}\Phi_J \right\rangle, \\ Y_{IJ}^k &= \left\langle \Phi_I \middle| \frac{\partial^2}{\partial R_k^2}\Phi_J \right\rangle \end{aligned} \qquad (4)$$

with $\hat{H}^{(\text{el})}$ denoting the electronic Hamiltonian. It is a common convention that the bra-ket notation used here demands integration over the electronic coordinates $\mathbf{r}$. The second order derivative terms Y_{IJ}^k in eqn (3) are quite often neglected because they are always accompanied by the small quantity $\hbar^2$.[40,41] The nuclear paths $\mathbf{R}(t)$ are driven by the force matrix F_{IJ}^k expressed as

$$\begin{aligned} F_{IJ}^k &= -\frac{\partial H_{IJ}^{(\text{el})}}{\partial R_k} - \sum_K \left(X_{IK}^k H_{KJ}^{(\text{el})} - H_{IK}^{(\text{el})} X_{KJ}^k \right) \\ &\quad + i\hbar \sum_l \dot{R}_l \left[\frac{\partial X_{IJ}^l}{\partial R_k} - \frac{\partial X_{IJ}^k}{\partial R_l} \right]. \end{aligned} \qquad (5)$$

The off-diagonal elements of F_{IJ}^k, if not zero, induce path-branching at every single time step. Therefore a theoretically infinite number of branching-paths are proliferated finally in the exact solutions of eqn (5). To avoid such a difficulty, various practical methods have been proposed.[39–41]

Among others, the so-called semiclassical Ehrenfest theory (SET) is the simplest approximation, which is also called the mean-field approximation, in which the force matrix of eqn (5) is averaged over the electron wavepacket in such a way that

$$\begin{aligned} \langle F_k \rangle &= \sum_{IJ} C_I^* F_{IJ}^k C_J = -\sum_{IJ} C_I^* \frac{\partial H_{IJ}^{(\text{el})}}{\partial R_k} C_J \\ &\quad - \sum_{IJ} C_I^* \left(X_{IK}^k H_{KJ}^{(\text{el})} - H_{IK}^{(\text{el})} X_{KJ}^k \right) C_J, \end{aligned} \qquad (6)$$

giving a single scalar force to drive a single path. If the basis set $\{\Phi_I(\mathbf{r};\mathbf{R})\}$ happens to be complete, eqn (6) is reduced to the form of the Hellmann–Feynman force

$$\langle F_k \rangle = -\left\langle \Psi_{\text{elec}} \middle| \frac{\partial \hat{H}^{(\text{el})}}{\partial R_k} \middle| \Psi_{\text{elec}} \right\rangle. \qquad (7)$$

Precisely speaking, the conventional SET does not include the second order derivative terms Y_{IJ}^k in eqn (3), which is widely applied in the literature.[42–46] Here in this particular study we also use the mean-field approximation. The use of this method is justified for our relatively short-time applications, typically shorter than 20 fs, and for the reason that the space of the active electronic configurations is very large (see below).

3.1.2 Quantities used for the analysis of nonadiabatic electron dynamics. As tools for analysis of electron wavepacket dynamics, we adopt the unpaired electron density $D(\mathbf{r})$ and electron flux $\mathbf{j}(\mathbf{r},t)$. The unpaired electron density $D(\mathbf{r})$ is defined as[47]

$$\begin{aligned} D(\mathbf{r}) &= 2\rho(\mathbf{r},\mathbf{r}) - \int \mathrm{d}\mathbf{r}'\rho(\mathbf{r},\mathbf{r}')\rho(\mathbf{r}',\mathbf{r}) \\ &= \sum_i n_i(2-n_i)|\lambda_i(\mathbf{r})|^2 \end{aligned} \qquad (8)$$

at each nuclear position, in which $\rho(\mathbf{r},\mathbf{r}')$ is the first order spinless density matrix in the coordinate representation, and $\lambda_i(\mathbf{r})$ and n_i are the natural orbitals and their associated occupation numbers, respectively. $D(\mathbf{r})$ represents a spatial distribution of unpaired (radical) electrons, since the individual curve with

Open Access Article. Published on 30 March 2020. Downloaded on 2/8/2026 12:45:32 PM. This article is licensed under a Creative Commons Attribution 3.0 Unported Licence.

respect to n_i is convex upwards, with the singly occupied orbital (n_i = 1) marking the maximum. $D(\mathbf{r})$ can graphically represent radical generation and transfer, hole transfer, spatiotemporal redistribution of electron correlation,[47] and so on. The number of unpaired electrons N_D is naturally given as

$$N_{\mathrm{D}} = \int \mathrm{d}\mathbf{r} D(\mathbf{r}). \tag{9}$$

The regional unpaired electron population,[18] denoted as $N_{\mathrm{D}}^{\mathrm{L}}$, is defined as the sum of the atomic unpaired electron population assigned to such methods as Mulliken[48] and Löwdin[49] atomic population analyses. The difference N_{D}–$N_{\mathrm{D}}^{\mathrm{L}}$ will be used to illustrate radical transfer in space-time.

The electron flux $\mathbf{j}(\mathbf{r},t)$ (also referred to as the Schiff probability current density of electrons[50]) satisfies

$$\mathbf{j}(\mathbf{r},t) = \frac{\hbar}{2im_{\mathrm{e}}}\left[\nabla_{\mathbf{r}}\rho(\mathbf{r}',\mathbf{r}) - \nabla_{\mathbf{r}'}\rho(\mathbf{r}',\mathbf{r})\right]\bigg|_{\mathbf{r}'\to\mathbf{r}}, \tag{10}$$

for many-electron systems, where $\nabla_{\mathbf{r}}$ and $\nabla_{\mathbf{r}'}$ are the nabla with respect to $\mathbf{r}$ and $\mathbf{r}'$, respectively, and m_{e} is the electron mass. The flux satisfies the equation of continuity and therefore represents well the flow line of electrons induced by chemical reactions.[29,51–59] Despite the fact that the flux arising from core orbitals is not important in the interpretation of chemical reactions, they generally tend to appear with very large values. We therefore intentionally ignore the core-electron flux to focus on the valence orbital contribution in this paper.

3.1.3 Computational details. The matrix elements required for the nonadiabatic electron wavepacket dynamics are calculated with our implemented programs in the GAMESS package.[60,61] As the atomic orbital (AO) basis set, the Stevens, Basch, Krauss, Jasien, and Cundari effective core potentials (SBKJC ECPs)[62] are employed for Mn and Ca, while Pople's 6-31G is for the other atoms. No diffuse function has been added in the present study due to a heavy computational load and moreover since we do not have to treat the Rydberg states on N atoms in contrast to photoexcited charge separation.[17–19,21,22,29] No polarization functions are added either to the atomic basis set. However, our experience shows that the polarization functions do not bring about a significant effect on the qualitative description of the mechanisms.[18,19]

In the present nonadiabatic electron wavepacket dynamics calculations, the adiabatic electronic wavefunctions attained at each molecular geometry are employed as the basis functions $\{\Phi_I\}$ to expand the electron wavepacket Ψ_{elec}. These adiabatic states are tracked on-the-fly along the relevant nuclear paths. To do so, the state-averaged multi-configurational self-consistent field (SA-MCSCF)[63,64] level of calculations has been employed.

It should be noted that a sudden change of their characters can occur before and after the passage of nonadiabatic regions, which can destruct the time-continuity of Ψ_{elec}. To keep the appropriate ordering of the suffix I of Φ_I faithfully, we make use of the approximate overlap integrals of the electronic wavefunctions between a time step t and that of one-step before $t - \Delta t$.

The level of calculations, spin-multiplicity $2S + 1$, and excluded subsystems are summarized in Table 2. The total charge is commonly set to be neutral. $2S + 1$ is determined so that the Mn_4Ca oxo complex is in a high-spin state in terms of the number of electrons in the Mn 3d orbitals, which is usually the most stable in energy. The number of 3d orbitals required to describe the Mn atoms is estimated by using the conventional formal oxidation states (*e.g.*, Ca^{2+}, O^{2-}, OH^-, and $HCOO^-$). The unpaired electron of the phenoxy radical is assumed to have the opposite spin to those of the Mn oxo complex, so that closed-shell phenol is finally formed in the active space. Charge neutralization is assured by summing up the formal charge of typical atoms or molecules excluding Mn, and assuming that oxidation and reduction are compensated only by Mn atoms. The remaining electrons occupying Mn 4s and/or 3d orbitals determine the spin multiplicity. This is a standard way frequently used in the context of inorganic chemistry and works very well to predict or understand reactions. The singly-occupied natural orbitals calculated for a multi-nuclear Mn oxo complex at the SA-MCSCF level occasionally include mixed states of Mn 3d and other orbitals such as O 2p orbitals. Later, we study a relation between the oxidation number and the number of unpaired electrons.

3.2 Nonadiabatic electron wavepacket dynamics

3.2.1 Initial conditions. To obtain statistically meaningful data, the initial conditions for the dynamics should be sampled from appropriate distribution functions. However, such path samplings would be unpractical in the present study, because it

Table 2 Computational settings for the processes of charge separation and reloading. Nonadiabatic electron wavepacket dynamics at the SA-MCSCF level is performed for the charge separation (CS), whereas *ab initio* molecular dynamics (AIMD) at the UHF level is for the reloading (RL). $2S + 1$ indicates the spin multiplicity, in which $S\hbar$ is the total spin angular momentum. The components listed in the "Excluded" column are excluded from the model system for the present computations, because no qualitative effects are expected. Note also that XEA and XPA are commonly excluded from all the model systems. "SA(*X*)-CASSCF(*Y*e,*Z*o)" means *X* state-averaged complete active-space self-consistent field with *Y* electrons in *Z* orbitals. We average all the states so that *X* is equal to the number of CSFs used

Subprocess	$2S + 1$	Charge	Level of calculation	Excluded
$K_{01} \rightarrow K_{02}$: CS(1)	20	+1	SA(440)-CASSCF(21e,21o)	$Ca(HCOO)_2(H_2O)_2$
$K_{04} \rightarrow K_{05}$: RL(1)	21	0	UHF	EA, PA, H_2O
$K_{11} \rightarrow K_{12}$: CS(2)	19	+1	SA(399)-CASSCF(20e,20o)	$Ca(HCOO)_2(H_2O)_2$
$K_{14} \rightarrow K_{15}$: RL(2)	20	0	UHF	EA, PA, H_2O
$K_{21} \rightarrow K_{22}$: CS(3)	18	+1	SA(360)-CASSCF(19e,19o)	$Ca(HCOO)_2(H_2O)_2$
$K_{24} \rightarrow K_{25}$: RL(3)	19	0	UHF	EA, PA, H_2O
$K_{31} \rightarrow K_{32}$: CS(4)	17	+1	SA(323)-CASSCF(18e,18o)	$Ca(HCOO)_2(H_2O)_2$

Open Access Article. Published on 30 March 2020. Downloaded on 2/8/2026 12:45:32 PM. This article is licensed under a Creative Commons Attribution 3.0 Unported Licence.

costs much to calculate even a single SET path with the on-the-fly SA-MCSCF. Instead, we focus on the qualitative properties of the proton and electron coupled dynamics of specific paths that pass through nonadiabatic regions, which are found among the ground state and some low-lying excited states for the charge separation and the reloading subprocesses. We calculate SET paths of the collision-induced CPEWT to demonstrate the essential part of charge separation due to electron transfer from $Mn^{(4)}$ of EPD to EA ($K_{n1} \rightarrow K_{n2}$ with $n = 0, 1, 2, 3$). Here we will graphically highlight only one path for each charge separation, whose initial condition is set to surely pass through the non-adiabatic region with as low a kinetic energy as possible. Non-adiabatic interactions emerge more or less along those paths. Path-branchings are required in principle, but we only perform SET dynamics here, because we herein focus on the qualitative aspects of nonadiabatic electron dynamics. Besides, the time duration of the dynamics calculations is set to be short enough, typically 10 fs.

It is very difficult to calculate an SET path at the SA-MCSCF level for the reloading mechanisms, because too many CSFs are necessary even for a qualitative description of the mechanism. The critical difficulty lies in the time-evolution of the occupation number of the Mn 3d orbital and/or O 2p orbital of the tetra-nuclear Mn oxo complex. In the charge separation dynamics, these orbitals are fixed to be inactive (up to doubly-occupied) or virtual (unoccupied) orbitals, and thus the number of CSFs is kept small enough for practical computations yet large enough for a qualitative description of the mechanism.

Taking the first reloading process RL(1) in $K_{04} \rightarrow K_{05}$ as an example, the 3d orbitals of all the four Mn atoms, 2p orbitals of the three μ-hydroxo O atoms, and 4s orbitals of the $Mn^{(4)}$ atom should be included in the active space. However, if the spin multiplicity $2S + 1$ is set to be equal to 20 (the high-spin state), the number of CSFs becomes 552 000, which is a far from practical computation of on-the-fly SA-MCSCF along the paths. We therefore have tested a number of large active spaces within the computationally practical range, but none of them is sufficient for a qualitative description of the mechanism. Therefore we could not avoid abandoning the SA-MCSCF calculations for the electron wavepacket analysis of the mechanism of reloading. Instead, we use the unrestricted Hartree–Fock (UHF) level of calculation to find places for the electronic state of the reactant to undergo a transition to that of the product in the reloading processes. It is also found that these ''diabatic'' states (see below for the implication of the present diabaticity) have a crossing point like a conical intersection along the path of proton relay-transfer in reloading. When such a crossing appears, our *ab initio* molecular dynamics is designated to keep tracking on the ground state alone. Accordingly, the conservation of the total energy is violated to a little extent in passing through such "conical intersections". No remedy to retrieve the conservation has been made in this paper. More about the choice of the initial condition is described in Section S1 of the ESI.†[65]

3.3 Charge separation dynamics, energetics of reloading, and oxygen molecule formation

3.3.1 Transition from the K_0 state. We begin with the first charge separation (CS(1) in $K_{01} \rightarrow K_{02}$) to consider the series of reactions along the present water-splitting cycle. The state of the electron–proton donor is symbolically represented as H_3–EPD–H. This means that three protons and electrons lie on the skewed cubic Mn_3O_4 oxo complex, as stated above, whereas one proton and one electron sit on $Mn^{(4)}(O)(H_2O)_2$. Selected snapshots of the spatial distribution of the unpaired electron density $D(\mathbf{r})$ and the electron flux $\mathbf{j}(\mathbf{r})$ along the illustrated SET path running on the ground-state are shown in Fig. 12a.

At time t = 0.0 fs, relatively high $D(\mathbf{r})$ is found on EA = 4-methylphenol. This situation corresponds to PSII with $Y_Z^{\bullet}$ (the TyrZ radical) before the hole transfer to the Mn_4CaO_5

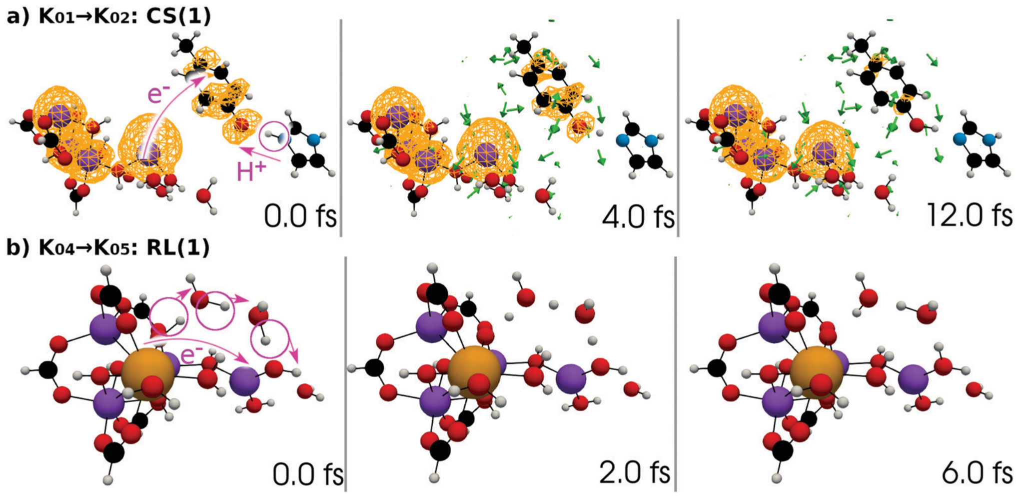

Fig. 12 (a) Selected snapshots of the spatial distribution of the unpaired electron density $D(\mathbf{r})$ (yellow contour mesh) and electron flux $\mathbf{j}(\mathbf{r})$ along a SET path of $K_{01} \rightarrow K_{02}$: CS(1) (SA-MCSCF level). See Fig. 4 for the corresponding chemical scheme. (b) Selected snapshots of an AIMD path of $K_{04} \rightarrow K_{05}$: RL(1) (UHF level). See Fig. 5 for the corresponding chemical scheme. Note that the time t = 0.0 fs is set to the starting time of the dynamics independently, and there is a somewhat long interval between the two subprocesses (a and b).

Open Access Article. Published on 30 March 2020. Downloaded on 2/8/2026 12:45:32 PM.
This article is licensed under a Creative Commons Attribution 3.0 Unported Licence.

cluster. As the proton on PA = imidazole is transferred to EA, $D(\mathbf{r})$ on EA gradually decreases as seen in the panels of $t = 4.0$ fs and $t = 12.0$ fs of Fig. 12a. This indicates that EA turns into a closed-shell state (*i.e.*, 4-methylphenol) as a result of this collision-induced CPEWT. The electron to be transferred should be assigned to be sitting in the 4s orbital of $\mathrm{Mn}^{(4)}$. Indeed $D(\mathbf{r})$ on this orbital decreases prominently as compared to the other orbitals. The electron flux $\mathbf{j}(\mathbf{r})$ also supports this view, since the flux is found only around the area near EA and $\mathrm{Mn}^{(4)}$. This type of mechanism has already been established in the study on a mononuclear Mn oxo complex.[20]

It is seen in Fig. 13a that a nonadiabatic transition occurs along the path among the quasi-degenerate adiabatic states. The figure shows the time evolution of potential energy curves V_I and state populations $|C_I|^2$ along the path. The population of the ground state at $t = 12.0$ fs is equal to 59% in this CS(1) [$\mathrm{K}_{01} \rightarrow \mathrm{K}_{02}$]. This implies that the electron wavepacket includes about 40% of the character of the reactant state (character having a radical on EA) even after passing through the non-adiabatic region. If path-branching is invoked, the path assigned to the reactant electronic state would easily induce the backward proton transfer (EA → PA), as we have shown for the excited-state charge separation.[18]

The natural orbitals of the MCSCF active space for CS(1) in $\mathrm{K}_{01} \rightarrow \mathrm{K}_{02}$ can be categorized into three types, namely,

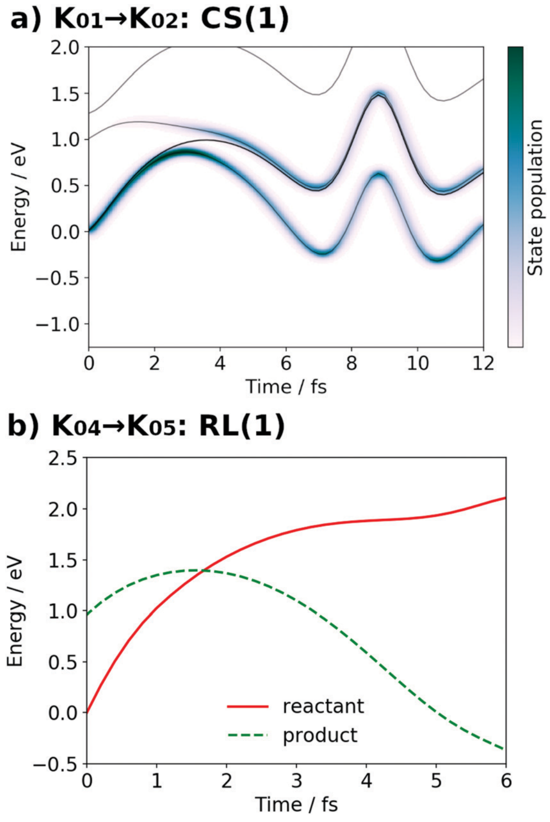

Fig. 13 (a) Potential energy curves V_I (solid line) and state population $|C_I|^2$ (pseudo-color map) along the SET path of $\mathrm{K}_{01} \rightarrow \mathrm{K}_{02}$: CS(1) (SA-MCSCF level). (b) Potential energy curves V_I for the reactant (solid line) and product (dashed line) along the AIMD path of $\mathrm{K}_{04} \rightarrow \mathrm{K}_{05}$: RL(1) (UHF level).

$\mathrm{3d/2p(Mn_4O_5)}$, $\mathrm{4s(Mn^{(4)})}$, and π(EA), in which the expression "(X)" indicates that the orbitals belong to the atom or molecule X. Again, $\mathrm{4s(Mn^{(4)})}$ indicates the 4s orbital of $\mathrm{Mn}^{(4)}$, which is responsible for the charge separation. Here $\mathrm{3d/2p(Mn_4O_5)}$ denotes the superposition of the 3d(Mn) and 2p(O) orbitals of the $\mathrm{Mn_4O_5}$ oxo complex.

It makes no sense to attempt to further assign the natural orbitals of this type to a specific atom. Note that the 4s orbitals of $\mathrm{Mn}^{(1)}$ through $\mathrm{Mn}^{(3)}$ (in the "3" part of the 3 + 1 structure) are not occupied throughout the present water-splitting cycle. Thanks to this feature, the present series of charge separation dynamics is carried out consistently and robustly. Thus the active-space configuration of the reactant state can be summarized as

$$(\mathrm{3d/2p(Mn_4O_5)})^{19}(\mathrm{4s(Mn^{(4)})})^{1}(\pi(\mathrm{EA}))^{1} \qquad (11)$$

with $2S + 1 = 20$. The typical configuration of the active space corresponding to the initial condition is thus rewritten in short-hand symbols as

$$\begin{array}{ccc} \mathrm{3d/2p(Mn_4O_5)} & \mathrm{4s(Mn^{(4)})} & \pi(\mathrm{EA}) \\ \hline \upharpoonleft \times 19 & \upharpoonleft & \downharpoonright \end{array} \qquad (12)$$

Here the top row shows the type of orbitals, whereas the bottom one shows the occupation number over the corresponding orbitals. For instance, "↿", "⇂", and "—" denote a singly occupied alpha-spin, a singly occupied beta-spin, and unoccupied orbitals, respectively. If N orbitals are categorized into the same type, they are arranged in the same column and abbreviated as "↿ × N". Likewise, "↿ × 3" ≡ "↿↿↿". The collision-induced CPEWT passing through the nonadiabatic region results in the following configuration

$$\begin{array}{ccc} \mathrm{3d/2p(Mn_4O_5)} & \mathrm{4s(Mn^{(4)})} & \pi(\mathrm{EA}) \\ \hline \upharpoonleft \times 19 & - & \upharpoonleft\downharpoonright \end{array} \qquad (13)$$

Here "↿⇂" denotes a doubly-occupied orbital. The product state is realized by the electron transfer from the $\mathrm{3d(Mn^{(4)})}$ orbital to π(EA). This reaction is regarded as a reaction changing from a biradical state to a closed-shell state, which is consistent with the time evolution of $D(\mathbf{r})$ as seen in Fig. 12. This assignment of the configuration may be oversimplified, yet it is useful for a visual understanding of the electronic states behind the dynamics. The other natural orbitals used below are referred to in the same manner. Hereafter, we refer to the "typical configuration of the active space" simply as the "initial conditions".

Next, the electronic state analysis along the AIMD path of RL(1) in $\mathrm{K}_{04} \rightarrow \mathrm{K}_{05}$ at the UHF level (Fig. 12b) supports the view of reloading in the scheme (see Fig. 5). As shown in Fig. 14, the UHF calculation along the path has converged to two states in this case (but not always) with two appropriate choices of initial guess of molecular orbitals (MOs). The total energies calculated with different initial guesses of MOs interchange along the AIMD path as seen in Fig. 13b. This suggests that electron transfer occurs along the path by passing through the non-adiabatic region generated by these two UHF states. We anticipate that such nonadiabatic electron wavepacket dynamics should take place there, if we can practically perform it.

Open Access Article. Published on 30 March 2020. Downloaded on 2/8/2026 12:45:32 PM. This article is licensed under a Creative Commons Attribution 3.0 Unported Licence.

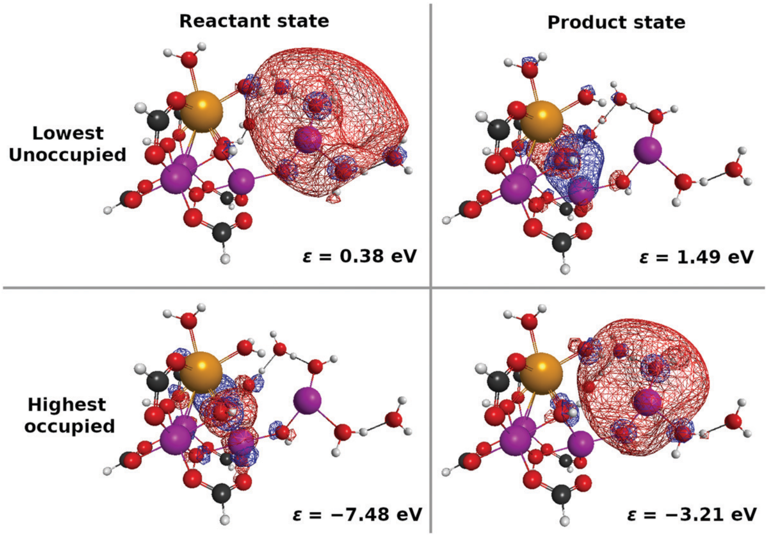

Fig. 14 Selected alpha-spin molecular orbitals (MOs) obtained for the initial molecular geometry of the dynamics of RL(1) in $K_{04} \rightarrow K_{05}$. Depending on the choice of the initial guess of MOs, the UHF calculation converges to two different sets of MOs, one having the nature of the reactant state and the other having the nature of the product state. These electronic states are characterized in terms of the occupancy of the $4s(Mn^{(4)})$ orbital: it is occupied and unoccupied in the product and the reactant states, respectively. In the case of the reactant state, the highest occupied alpha-spin MO is assigned to the $3d/2p(Mn_4CaO_5(H_2O)_2)$ orbital, whereas it becomes the lowest unoccupied in the product state. This suggests that electron transfer indeed occurs from the "3" part to the "1" part of the "3 + 1" structure. The $3d/2p(Mn_4CaO_5(H_2O)_2)$ orbital is seen to be dominated by the 2p(O) orbital, which also serves as the source of a proton. The same tendency is found for RL(2) in $K_{14} \rightarrow K_{15}$ and RL(3) in $K_{24} \rightarrow K_{25}$ as well.

The UHF calculation along with our experience suggests the possible configuration of the active space corresponding to the initial condition of RL(1) in $K_{04} \rightarrow K_{05}$ as

$$\begin{array}{cc} \underline{3d/2p(Mn_4CaO_7)} & \underline{4s(Mn^{(4)})} \\ \upharpoonleft \times 19 & - \end{array} \tag{14}$$

Note that $3d/2p(Mn_4CaO_7)$ denotes a superposition of Mn and/or Ca 3d orbitals and O 2p orbitals of the $Mn_4CaO_5(H_2O)_2$ cluster, in which two H_2O molecules are bound to the Ca atom. Similarly, the product state of the reloading should be as

$$\begin{array}{cc} \underline{3d/2p(Mn_4CaO_7)} & \underline{4s(Mn^{(4)})} \\ \upharpoonleft \times 18 & \upharpoonleft \end{array} \tag{15}$$

This reaction reloads an electron into the $4s(Mn^{(4)})$ orbital and a proton onto $Mn^{(4)}$–OH, which enables the next charge separation. The notion of reloading has been extensively explored in our previous study on the binuclear Mn oxo complex.[22]

3.3.2 Transition from the K_1 state. The results of the second charge separation dynamics, namely, CS(2) in $K_{11} \rightarrow K_{12}$, are qualitatively the same as CS(1) in $K_{01} \rightarrow K_{02}$. The state of the electron–proton donor is now represented as H_2–EPD–H. Here in this stage the formal oxidation state of the skewed cubic $Mn_3CaO_4(H_2O)_2$ has increased by one. Nevertheless, the electronic state of $Mn^{(4)}(OH)(H_2O)_2$ remains almost the same, so that the charge separation occurs in qualitatively the same manner. Selected snapshots of the unpaired electron density $D(\mathbf{r})$ and the electron flux $\mathbf{j}(\mathbf{r})$ are shown in Fig. 15a. At time $t = 0.0$ fs, $D(\mathbf{r})$ is seen on EA, indicating that there exists a 4-methylphenoxy radical. Then it turns into a closed-shell molecule (*i.e.*, 4-methylphenol), coupling to the PA to EA proton transfer. As shown in Fig. 16, the time-evolution of the potential energy curves V_I and their population $|C_I|^2$ also has the same tendency as those of CS(1) in $K_{01} \rightarrow K_{11}$ (Fig. 16a). The ground-state population at $t = 12.0$ fs is equal to 68%.

The interpretation of the dynamics can be given in terms of the active space configurations as follows. The initial condition is written as

$$\begin{array}{ccc} \underline{3d/2p(Mn_4O_5)} & \underline{4s(Mn^{(4)})} & \underline{\pi(EA)} \\ \upharpoonleft \times 18 & \upharpoonleft & \downharpoonright \end{array} \tag{16}$$

The collision-induced CPEWT passing through the nonadiabatic region results in the following configuration

$$\begin{array}{ccc} \underline{3d/2p(Mn_4O_5)} & \underline{4s(Mn^{(4)})} & \underline{\pi(EA)} \\ \upharpoonleft \times 18 & & \upharpoonleft\downharpoonright \end{array} \tag{17}$$

These results of the second charge separation indicate that the sequential charge separations can materialize in this stage without oxidizing a water molecule. A similar situation has been seen in the excited-state charge separation with the binuclear Mn oxo complex.[22]

We can readily guess that the possible configuration of the active space corresponding to the initial condition of RL(2) in $K_{14} \rightarrow K_{15}$ should be

$$\begin{array}{cc} \underline{3d/2p(Mn_4CaO_7)} & \underline{4s(Mn^{(4)})} \\ \upharpoonleft \times 18 & - \end{array} \tag{18}$$

and the reactant state as well should be as

$$\begin{array}{cc} \underline{3d/2p(Mn_4CaO_7)} & \underline{4s(Mn^{(4)})} \\ \upharpoonleft \times 17 & \upharpoonleft \end{array} \tag{19}$$

This reaction again reloads an electron into the $4s(Mn^{(4)})$ orbital and a proton on $Mn^{(4)}$–OH, which makes the next charge separation possible.

Open Access Article. Published on 30 March 2020. Downloaded on 2/8/2026 12:45:32 PM. This article is licensed under a Creative Commons Attribution 3.0 Unported Licence.

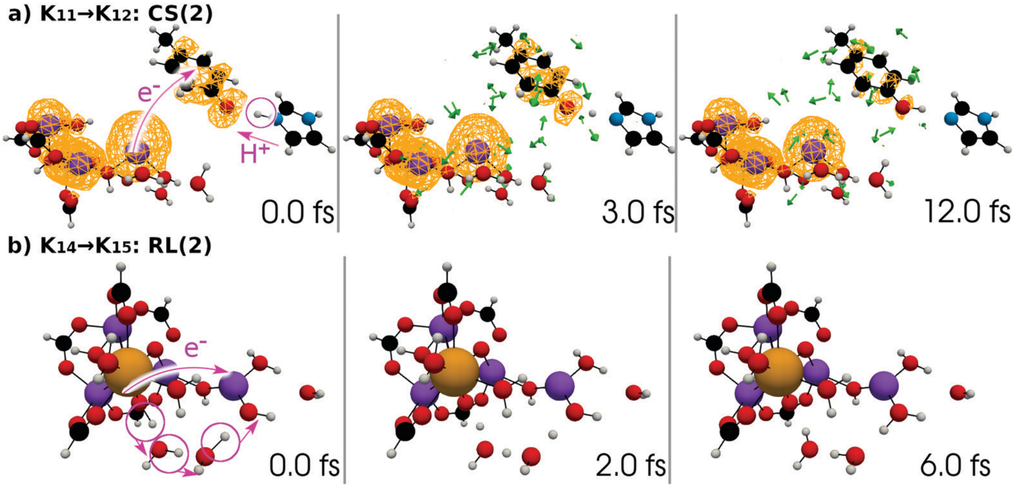

Fig. 15 (a) Selected snapshots of the spatial distribution of the unpaired electron density $D(\mathbf{r})$ (yellow contour mesh) and electron flux $\mathbf{j}(\mathbf{r})$ along a SET path of $K_{11} \rightarrow K_{12}$: CS(2) (SA-MCSCF level). See Fig. 6 for the corresponding chemical scheme. (b) Selected snapshots of an AIMD path of $K_{14} \rightarrow K_{15}$: RL(2) (UHF level). See Fig. 7 for the corresponding chemical scheme. Note that the time t = 0.0 fs is set to the starting time of the dynamics independently, and there is a somewhat long interval between the two subprocesses (a and b).

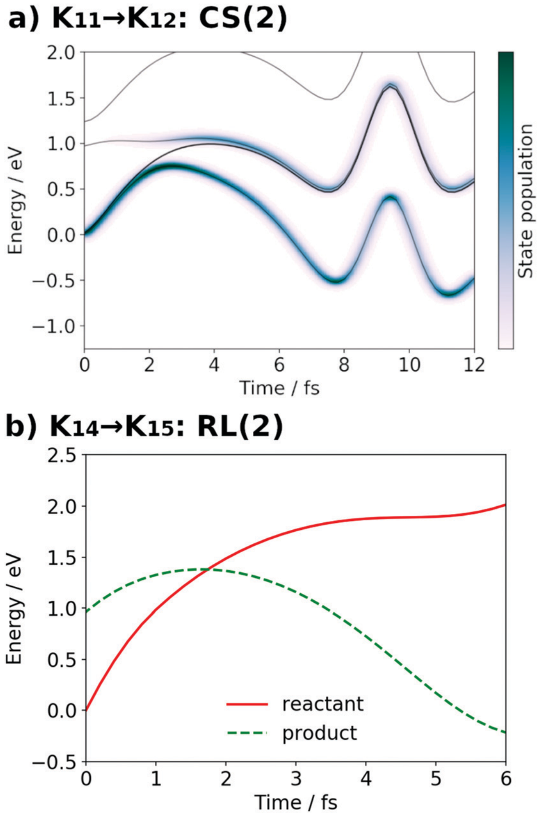

Fig. 16 (a) Potential energy curves V_I (solid line) and state population $|C_I|^2$ (pseudo-color map) along the SET path of $K_{21} \rightarrow K_{22}$: CS(2) (SA-MCSCF level). (b) Potential energy curves V_I for the reactant (solid line) and product (dashed line) along the AIMD path of $K_{24} \rightarrow K_{25}$: RL(2) (UHF level).

3.3.3 Transition from the K_2 state. In contrast to the binuclear Mn oxo complex,[22] the present tetranuclear Mn oxo complex can proceed to further charge separation without water oxidation. The results of the third charge separation dynamics, namely, CS(3) in $K_{21} \rightarrow K_{22}$, are qualitatively the same as CS(2) in $K_{11} \rightarrow K_{12}$ and CS(1) in $K_{01} \rightarrow K_{02}$. The state of the electron–proton donor is now reduced to H–EPD–H. Compared to the initial state, that is, H_3–EPD–H, the formal oxidation state of the skewed cubic $Mn_3CaO_4(H_2O)_2$ complex has further increased by two. As shown below, although the formal oxidation state is different from the previous two charge separations, the electronic state of $Mn^{(4)}$–OH is found to still remain almost the same. Selected snapshots of the unpaired electron density $D(\mathbf{r})$ and the electron flux $\mathbf{j}(\mathbf{r})$ are shown in Fig. 17a.

At time t = 0.0 fs, $D(\mathbf{r})$ is seen on EA, indicating that there exists a 4-methylphenoxy radical. Then it turns into a closed-shell species (*i.e.*, 4-methylphenol), coupling with the PA to EA proton transfer. As shown in Fig. 18a, the time-evolution of the potential energy curves V_I and their population $|C_I|^2$ also has the same tendency as those of CS(1) in $K_{01} \rightarrow K_{11}$ (Fig. 18a). The ground-state population at t = 12.0 fs is equal to 83%.

The charge separation dynamics can be interpreted in terms of the active space configurations, which are directly guessed from the UHF calculations. The initial condition is written as

$$\frac{3\mathrm{d}/2\mathrm{p}(\mathrm{Mn_4O_5})}{\upharpoonleft \times 17}\;\frac{4\mathrm{s}(\mathrm{Mn^{(4)}})}{\upharpoonleft}\;\frac{\pi(\mathrm{EA})}{\downharpoonright} \tag{20}$$

The collision-induced CPEWT passing through the nonadiabatic region results in the following configuration

$$\frac{3\mathrm{d}/2\mathrm{p}(\mathrm{Mn_4O_5})}{\upharpoonleft \times 17}\;\frac{4\mathrm{s}(\mathrm{Mn^{(4)}})}{-}\;\frac{\pi(\mathrm{EA})}{\upharpoonleft\downharpoonright} \tag{21}$$

We can also guess the possible configuration of the active space corresponding to the initial condition of RL(3) in $K_{24} \rightarrow K_{25}$ as

$$\frac{3\mathrm{d}/2\mathrm{p}(\mathrm{Mn_4CaO_7})}{\upharpoonleft \times 17}\;\frac{4\mathrm{s}(\mathrm{Mn^{(4)}})}{-} \tag{22}$$

Open Access Article. Published on 30 March 2020. Downloaded on 2/8/2026 12:45:32 PM. This article is licensed under a Creative Commons Attribution 3.0 Unported Licence.

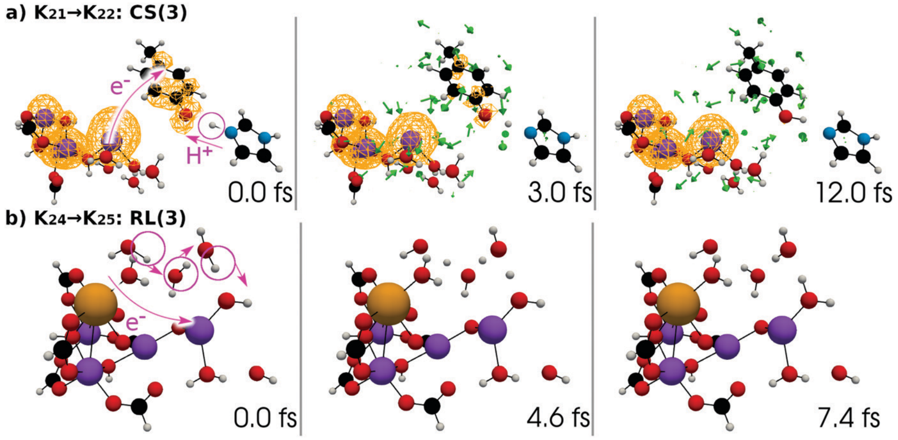

Fig. 17 (a) Selected snapshots of the spatial distribution of the unpaired electron density $D(\mathbf{r})$ (yellow contour mesh) and electron flux $\mathbf{j}(\mathbf{r})$ along a SET path of $K_{21} \rightarrow K_{22}$: CS(3) (SA-MCSCF level). See Fig. 8 for the corresponding chemical scheme. (b) Selected snapshots of an AIMD path of $K_{24} \rightarrow K_{25}$: RL(3) (UHF level). See Fig. 9 for the corresponding chemical scheme. Note that the time t = 0.0 fs is set to the starting time of the dynamics independently, and there is a somewhat long interval between the two subprocesses (a and b).

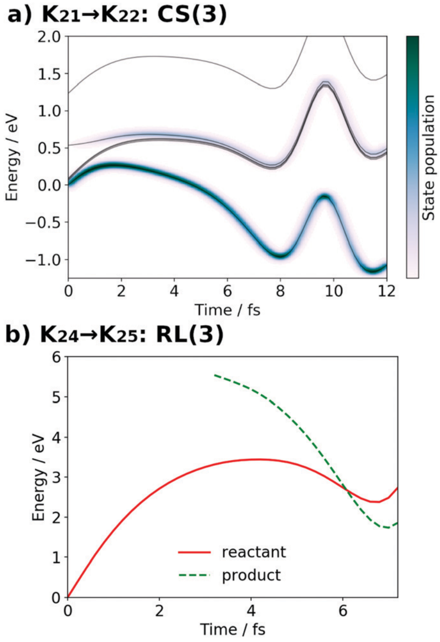

Fig. 18 (a) Potential energy curves V_I (solid line) and state population $|C_I|^2$ (pseudo-color map) along the SET path of $K_{21} \rightarrow K_{22}$: CS(3) (SA-MCSCF level). (b) Potential energy curves V_I for the reactant (solid line) and product (dashed line) along the AIMD path of $K_{24} \rightarrow K_{25}$: RL(3) (UHF level). The dashed line from t = 0.0 fs to t = 3.2 fs is not plotted, because convergence to the product state was not attained.

and the reactant state may be similarly speculated as

$$\frac{3\mathrm{d}/2\mathrm{p}(\mathrm{Mn_4CaO_7})}{\upharpoonleft \times 16}\ \frac{4\mathrm{s}(\mathrm{Mn}^{(4)})}{\upharpoonleft} \tag{23}$$

This reaction once again reloads an electron into the 4s($Mn^{(4)}$) orbital and a proton on $Mn^{(4)}$–OH, which enables the last charge separation in one circuit.

3.3.4 Transition from the K_3 state. The present tetranuclear Mn oxo complex can be further engaged in charge separation before water oxidation. The results of the fourth charge separation dynamics, namely, CS(4) in $K_{31} \rightarrow K_{32}$, are qualitatively the same as those of CS(1), CS(2), and CS(3). The state of the electron–proton donor is represented finally as EPD–H. Compared to the initial state, that is, H_3–EPD–H, the formal oxidation state of the skewed cubic $Mn_3CaO_4(H_2O)_2$ complex has increased by three. The electronic state of $Mn^{(4)}$–OH still remains almost the same as that of CS(1), CS(2), and CS(3), although the formal oxidation state is mutually different. Selected snapshots of the unpaired electron density $D(\mathbf{r})$ and the electron flux $\mathbf{j}(\mathbf{r})$ are shown in Fig. 19a. The ground-state population at t = 12.0 fs is equal to 83%.

At time t = 0.0 fs, $D(\mathbf{r})$ is seen on EA, indicating that there exists a 4-methylphenoxy radical. Then it turns into a closed-shell species (*i.e.*, 4-methylphenol), coupling with the PA to EA proton transfer. As shown in Fig. 20a, the time-evolution of the potential energy curves V_I and their population $|C_I|^2$ also has the same tendency as those of CS(1) in $K_{01} \rightarrow K_{11}$ (Fig. 20a).

$$\frac{3\mathrm{d}/2\mathrm{p}(\mathrm{Mn_4O_5})}{\upharpoonleft \times 16}\ \frac{4\mathrm{s}(\mathrm{Mn}^{(4)})}{\upharpoonleft}\ \frac{\pi(\mathrm{EA})}{\downharpoonright} \tag{24}$$

The collision-induced CPEWT passing through the nonadiabatic region results in the following configuration

$$\frac{3\mathrm{d}/2\mathrm{p}(\mathrm{Mn_4O_5})}{\upharpoonleft \times 16}\ \frac{4\mathrm{s}(\mathrm{Mn}^{(4)})}{-}\ \frac{\pi(\mathrm{EA})}{\upharpoonleft\downharpoonright} \tag{25}$$

Now that four charge separations have materialized, the system should be ready to complete one circuit of the catalytic cycle with molecular oxygen evolution as a by-product.

In this last stage, we have different dynamics other than the three reloading steps, RL(1) [K_{04}–K_{05}], RL(2) [K_{14}–K_{15}], and RL(3) [K_{24}–K_{25}]. A schematic representation of the final dynamics of water splitting has been illustrated in Fig. 11. Unfortunately, however, the AIMD dynamics with UHF, let alone the nonadiabatic electron dynamics, is too large in computational size to faithfully track the complicated electronic state transitions. This makes a large difference from the water oxidation by the binuclear Mn oxo complex. (As a matter of fact, nonadiabatic electron wavepacket

Open Access Article. Published on 30 March 2020. Downloaded on 2/8/2026 12:45:32 PM. This article is licensed under a Creative Commons Attribution 3.0 Unported Licence.

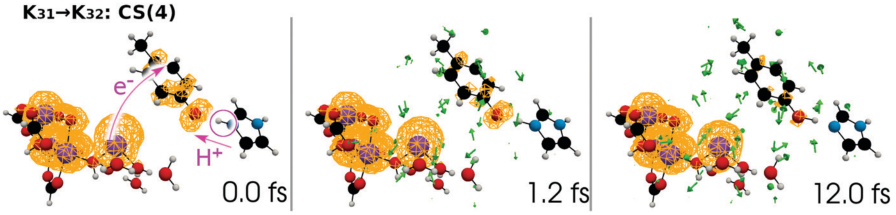

Fig. 19 Selected snapshots of the spatial distribution of the unpaired electron density $D(\mathbf{r})$ (yellow contour mesh) and electron flux $\mathbf{j}(\mathbf{r})$ along a SET path of $K_{31} \rightarrow K_{32}$: CS(4) (SA-MCSCF level). See Fig. 10 for the corresponding chemical scheme. This is the final charge separation in a single cycle. Mn reduction will follow this charge separation to complete one circuit.

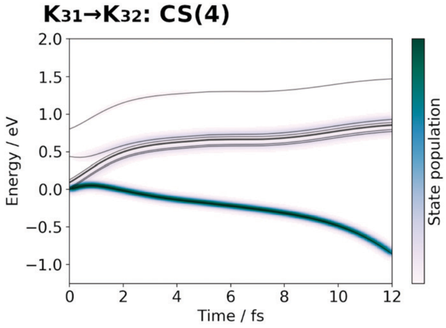

Fig. 20 Potential energy curves V_I (solid line) and state population $|C_I|^2$ (pseudo-color map) along the SET path of $K_{31} \rightarrow K_{32}$: CS(4) (SA-MCSCF level).

dynamics was carried out for the dynamics of the Mn-reduction process leading to the formation of a spin triplet oxygen molecule in photocatalytic water-splitting by the binuclear Mn oxo complex.[22]) We therefore can investigate the feasibility of one possible mechanism for water-oxidation only from the viewpoint of energetics. This aspect is visualized with an energy profile in the next subsection, in which not only the O_2 generation in the course of K_{35} to K_{37} but almost all the other processes are displayed together.

3.4 Energy profile

The dynamical analysis given above has been performed on selected processes such as the charge separation. However, we admit that those dynamical calculations are not long enough to track the connection from one dynamics to the next one. Moreover, such extensive dynamical analyses are technically prohibitive at present due to the extraordinarily severe computational cost. This is particularly the case for reloading dynamics. Besides, it is practically impossible to dynamically track the processes in K_{03} [Fig. 4], K_{13} [Fig. 6], K_{23} [Fig. 8], and K_{33} [Fig. 10], in which the relay-transferred proton is eventually handed over to an imagined external proton acceptor (XPA) such as P680. The far more challenging task to apply nonadiabatic electron wavepacket dynamics is the process of oxygen generation ranging from K_{34} to K_0 through K_{35}, K_{36}, and K_{37} [Fig. 11]. We admit that all we can do for these particular stages of the catalytic cycle is to estimate the static energies of the individual K_{nm}. With those energies, we here address the feasibility of the present water-splitting cycle.

The electronic energy values for the individual K_{nm} states, as displayed in Fig. 21, have been semiquantitatively estimated as follows. The total energy for each K_{nm} state is a sum of those of the components as shown in the column "Components" of Table 3, each individual component being specified in the square brackets. Those components are assumed to be separated (not physically but mathematically). The spin multiplicity is set to high-spin with respect to the formal oxidation state of the Mn atoms and OH radicals (if any) for the donor components. The spin multiplicity for the acceptor components is set to be either singlet or doublet depending on the state of EA. The total charge is determined from the schematic representation.

First, we define the molecular "components" that build up each metastable state through K_n and K_{nm}, the AO basis set of which is the same as that used in the dynamics calculations. (See from Fig. 4–11 for each molecular structure of the metastable states.) Note that XEA and XPA are commonly excluded from all the model molecular systems. Note also that the five HCOO groups in EPD are not displayed in the figures of the chemical schemes, although they are taken into account in the energy computation.

The electronic energy of each "component" has been evaluated after geometry optimization based on conventional quantum chemical calculations using the GAMESS program package.[60,61] The unrestricted Hartree–Fock (UHF) level of calculations is used so as to be consistent with the *ab initio* dynamics for the reloading. Accordingly the same atomic basis set is used, that is, the Stevens, Basch, Krauss, Jasien, and Cundari effective core potentials (SBKJC ECPs)[62] for Mn and Pople's 6-31G for the other atoms. The optimized energy of the components and that of triplet oxygen as well are tabulated in Section S2 of the ESI.† [65]

It is difficult to calculate the entire energy of the whole system shown in the chemical scheme, because biradical states are involved, whose energies tend to be overestimated with the UHF level. Moreover, there is no way to estimate the energy loss or gain at the boundary between EA (PA) and XEA (XPA), simply because we have neither XEA not XPA explicitly. Therefore the energy profile diagram of Fig. 21 is segmented into four natural pieces and the energies have been accordingly estimated as in Table 3. The energy profiles thus estimated should be compared within the individual partitions.

It is seen in Fig. 21 that the subprocess K_{22} seems to gives a relatively high barrier, but this reaction process is expected to proceed in a concerted manner with the low energy reaction of K_{23}.

Open Access Article. Published on 30 March 2020. Downloaded on 2/8/2026 12:45:32 PM. This article is licensed under a Creative Commons Attribution 3.0 Unported Licence.

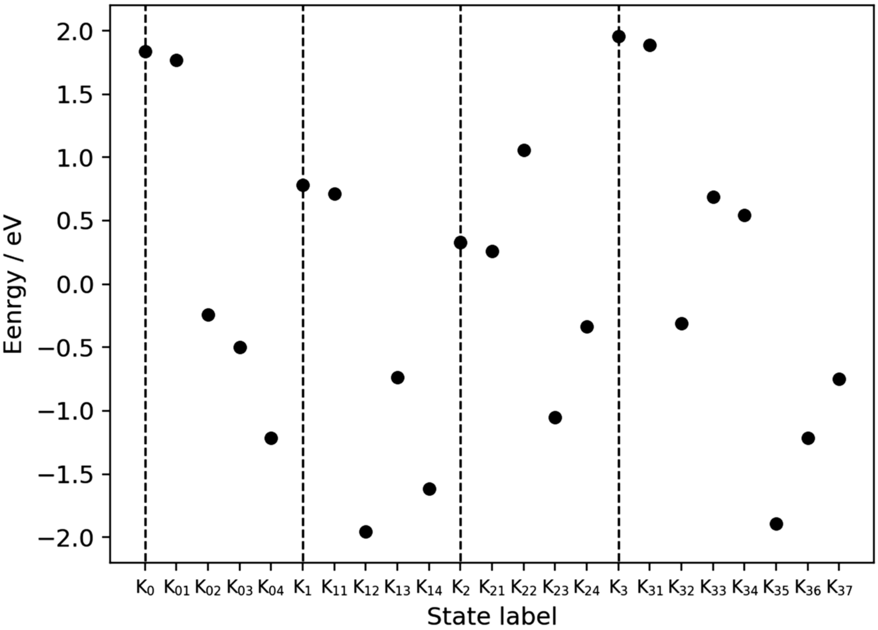

Fig. 21 Energy profile for the metastable states of the present water-splitting cycle. Table 3 shows how the energies have been estimated to be compared among the metastable states (K_n and K_{nm}), whose numbers of electrons and nuclei are mutually different. The baseline of the energy is set so that the average of all the points is equal to zero. The energies of K_{n5} are not displayed to save space, but they should be exactly or almost equal to K_{n+1} (n = 0, 1, 2). The total energy is calculated separately for the acceptor (EA and PA) and the other part including EPD, EPR, and some water molecules. The dashed vertical lines mark the positions of K_n (n = 0, 1, 2, 3).

Table 3 The energy of (metastable) states is estimated by summing up the electronic energies of the components indicated by the square brackets, which are calculated separately from each other. The superscript number on the left side on each component denotes the spin multiplicity, whereas that on the right side denotes the total charge. For example $^{1}[\text{EA–H + H–PA–H}]^{+}$ means that the subsystem consists of EA–H = 4-methylphenol and H–PA–H = imidazolium in the spin singlet and cationic state. It is assumed that the external electrons and protons are already accepted by XEA and XPA, respectively. We add the stabilization energy E_e of the electron on XEA as a parameter, which is set to E_e = −12.4 eV for each external electron. We also add a stabilization energy E_H = −4.9 eV for each external proton on XPA. These parameters are determined so as to minimize the variance of the energy distribution of all the points in Fig. 21

Metastable state	Components	External
K_0 (Fig. 4)	$^{21}[H_3\text{–EPD–H} + 3H_2O] + {}^{1}[\text{EA–H + PA–H}]$	$0e^- + 0H^+$
K_{01} (Fig. 4)	$^{21}[H_3\text{–EPD–H} + 3H_2O] + {}^{2}[\text{EA + H–PA–H}]^{+}$	$1e^- + 0H^+$
K_{02} (Fig. 4)	$^{20}[H_3\text{–EPD–H} + 3H_2O]^{+} + {}^{1}[\text{EA–H + PA–H}]$	$1e^- + 0H^+$
K_{03} (Fig. 4)	$^{20}[H_3\text{–EPD} + 3H_2O] + {}^{1}[\text{EA–H + H–PA–H}]^{+}$	$1e^- + 0H^+$
K_{04} (Fig. 5)	$^{20}[H_3\text{–EPD} + 3H_2O] + {}^{1}[\text{EA–H + PA–H}]$	$1e^- + 1H^+$
K_1 (Fig. 6)	$^{20}[H_2\text{–EPD–H} + 3H_2O] + {}^{1}[\text{EA–H + PA–H}]$	$1e^- + 1H^+$
K_{11} (Fig. 6)	$^{20}[H_2\text{–EPD–H} + 3H_2O] + {}^{2}[\text{EA + H–PA–H}]^{+}$	$2e^- + 1H^+$
K_{12} (Fig. 6)	$^{19}[H_2\text{–EPD–H} + 3H_2O]^{+} + {}^{1}[\text{EA–H + PA–H}]$	$2e^- + 1H^+$
K_{13} (Fig. 6)	$^{19}[H_2\text{–EPD} + 3H_2O] + {}^{1}[\text{EA–H + H–PA–H}]^{+}$	$2e^- + 1H^+$
K_{14} (Fig. 7)	$^{19}[H_2\text{–EPD} + 3H_2O] + {}^{1}[\text{EA–H + PA–H}]$	$2e^- + 2H^+$
K_2 (Fig. 8)	$^{19}[\text{H–EPD–H} + 3H_2O] + {}^{1}[\text{EA–H + PA–H}]$	$2e^- + 2H^+$
K_{21} (Fig. 8)	$^{19}[\text{H–EPD–H} + 3H_2O] + {}^{2}[\text{EA + H–PA–H}]^{+}$	$3e^- + 2H^+$
K_{22} (Fig. 8)	$^{18}[\text{H–EPD–H} + 3H_2O]^{+} + {}^{1}[\text{EA–H + PA–H}]$	$3e^- + 2H^+$
K_{23} (Fig. 8)	$^{18}[\text{H–EPD} + 3H_2O] + {}^{1}[\text{EA–H + H–PA–H}]^{+}$	$3e^- + 2H^+$
K_{24} (Fig. 9)	$^{18}[\text{H–EPD} + 3H_2O] + {}^{1}[\text{EA–H + PA–H}]$	$3e^- + 3H^+$
K_3 (Fig. 10)	$^{18}[\text{EPD–H} + 3H_2O] + {}^{1}[\text{EA–H + PA–H}]$	$3e^- + 3H^+$
K_{31} (Fig. 10)	$^{18}[\text{EPD–H} + 3H_2O] + {}^{2}[\text{EA + H–PA–H}]^{+}$	$4e^- + 3H^+$
K_{32} (Fig. 10)	$^{17}[\text{EPD–H} + 3H_2O]^{+} + {}^{1}[\text{EA–H + PA–H}]$	$4e^- + 3H^+$
K_{33} (Fig. 10)	$^{17}[\text{EPD} + 3H_2O] + {}^{1}[\text{EA–H + H–PA–H}]^{+}$	$4e^- + 3H^+$
K_{34} (Fig. 11)	$^{17}[\text{EPD} + 3H_2O] + {}^{1}[\text{EA–H + PA–H}]$	$4e^- + 4H^+$
K_{35} (Fig. 11)	$^{19}[\text{H–EPD(OOH)} + 2H_2O] + {}^{1}[\text{EA–H + PA–H}]$	$4e^- + 4H^+$
K_{36} (Fig. 11)	$^{19}[\text{H–EPD(OO)–H} + 2H_2O] + {}^{1}[\text{EA–H + PA–H}]$	$4e^- + 4H^+$
K_{37} (Fig. 11)	$^{21}[\text{H–EPD}(H_2O)\text{–H} + H_2O] + {}^{1}[\text{EA–H + PA–H}] + {}^{3}[O_2]$	$4e^- + 4H^+$

Open Access Article. Published on 30 March 2020. Downloaded on 2/8/2026 12:45:32 PM. This article is licensed under a Creative Commons Attribution 3.0 Unported Licence.

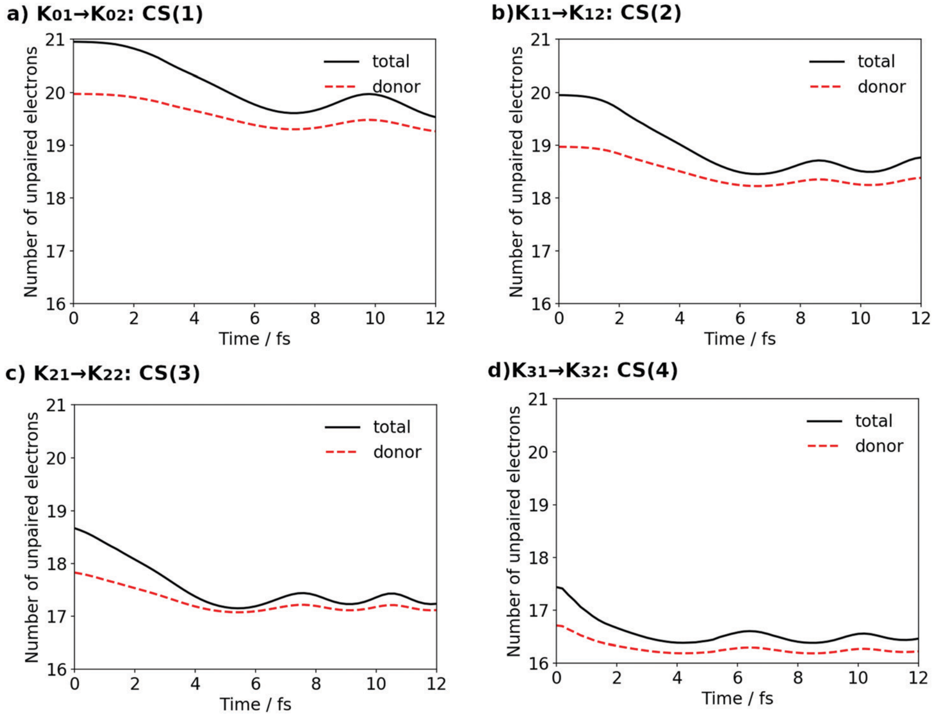

Fig. 22 The total number of unpaired electrons N_D (solid line) and the Löwdin regional unpaired electron population for the donor N_D^L (red broken line).

As described above, the final stage of our proposed catalytic cycle from K_{35} to K_{37} in Fig. 11, where two water molecules are split and triplet oxygen is formed, could not be treated dynamically, and only the energy diagram is available to discuss the feasibility of the model. Fig. 21 shows that the Mn reduction subprocesses (from K_{35} to K_{37}) seem to require as much as 1.5 eV to proceed. It is highly possible though that this barrier is lowered to some large extent by an expected interaction between the Mn reduction center and newly inserted water molecules, which can take place in a synchronous manner with O_2 evolution.

It is finally seen from the energy profile that there are no states of excessively high and low energy.

3.5 Unpaired electron numbers and oxidation numbers

Before concluding the numerical analyses, we track the dynamics of the oxidation states of the Mn cluster on each occasion of the four-step charge separation. To do so without the use of the formal oxidation number, the definition of which is somewhat obscure, we here illustrate the time-evolution of the total number of unpaired electrons N_D, which is accumulated from all over the system, and compare it with the Löwdin regional unpaired electron population N_D^L for the part of the electron and proton donor (EPD) only. Both N_D and N_D^L are time-dependent and their graphs are shown in Fig. 22 for all the four charge separation dynamics.

Each panel in the figure demonstrates that N_D^L for EPD at each $t = 0.0$ of CS(1) [K_{01}], CS(2) [K_{11}], CS(3) [K_{21}] and CS(4) [K_{31}], respectively, decreases one by one as the formal oxidation state proceeds, reflecting that one electron is transported to XEA on each occasion of charge separation.

The difference between N_D and N_D^L in each panel at $t = 0.0$ shows that there is one radical electron in EA (see for instance K_{01} in Fig. 4 after the contact with EA0 (Fig. 3)). This difference tends to converge to zero as the time of the charge separation process proceeds, since a singly-occupied natural orbital in EA, which corresponds to the 4-methylphenoxy radical, is further occupied by another electron that is transported from EPD (Mn cluster). Thus this natural orbital becomes nearly doubly occupied and the radical disappears. (Note however that the differences do not converge exactly to zero in all the cases, mainly because the unpaired electrons reflect also the effects from electron correlation and/or other nonadiabatic interactions.) After some short time, say 12 fs, the unpaired electrons are thus found in the EPD part only. Besides, population analysis shows that the electron loss from EPD is mainly due to the transfer from the 4s-like state on $Mn^{(4)}$, and this 4s-like state is seen to be refilled by an electron from the cubic structure after the reloading process.

Thus the graphs in Fig. 22 suggest that the decrease of the unpaired electrons due to reloading can be linked to the increase of the "oxidation number" of the entire skewed cubic structure (but not to the individual constituent Mn atoms). In fact the combination of N_D and N_D^L has well represented the time-variation of the oxidation process. Thus Fig. 22 together with Fig. 12, 15, 17 and 19 clearly evidences that the electrons used in the four charge separation dynamics are consistently launched solely from $Mn^{(4)}$.

4 Concluding remarks

We have theoretically studied a catalytic cycle as a possible model of water splitting in PSII. The catalyst we chose is

Open Access Article. Published on 30 March 2020. Downloaded on 2/8/2026 12:45:32 PM. This article is licensed under a Creative Commons Attribution 3.0 Unported Licence.

$Mn_4Ca(OH)_5(HCOO)_5(H_2O)_4$ tied with an electron acceptor (4-methylphenol as a model compound D1-Y161 or TyrZ (Y_Z)) and also with a proton acceptor (imidazole as a model compound of D1-H190 or HisZ). These molecules are connected through hydrogen bonds due to water clusters. This Mn cluster is appropriately divided as $Mn_3Ca(H_2O)_2(OH)_4$–OH–$Mn^{(4)}(H_2O)_2$, where the skewed cubic geometric structure including Mn_3CaO_4 is fastened by five carboxy groups. Charge separation processes, through which protons and electrons are extracted and transported to the acceptors, have been extensively studied in terms of nonadiabatic electron wavepacket dynamics as the predominantly vital process in biological systems. What we have performed and observed are summarized as follows.

We first regard that the present water splitting cycle is triggered by ground-state collision (contact) induced charge separation (chemi-charge-separation). As stated in the Introduction, this is never a trivial assertion, since only the photoinduced charge separation mechanism had been studied quantum mechanically before our concrete identification.[20] In collision-induced dynamics, the long time-scale of the total dynamics is determined by the product of the collision frequency and reaction probability at each collision, while the elementary processes such as charge separation are very fast down to the scale of femtoseconds.

As for the molecular geometry, we assumed that the relative orientation of the Mn cluster and the electron and proton acceptors remains loosely fixed. We identify a reaction field in a rather large open space which is surrounded by $Mn^{(4)}$, $O^{(4)}$, $Mn^{(3)}$, $O^{(2)}$, $O^{(5)}$, and Ca. External water molecules are invited into this space, which serve as media of proton relay-transfer at one time and undergo decomposition in other situations.

Then the following phenomena throughout the cycle have been clarified:

(I) Charge separation dynamics, in which the supply of electrons and protons to the acceptors occurs, turns out to be performed four times exclusively through the moiety of $Mn^{(4)}(H_2O)_2$ throughout the cycle. The diffuse 4s-like state on $Mn^{(4)}$ is found to be responsible for the electron transfer from the cluster to the electron acceptor.

(II) For this charge-separation dynamics (electron–proton donation from the cluster) to be successfully repeated, intramolecular reconfigurations of the electronic and protonic states should follow appropriately to compensate the loss of electrons and protons, which we called the reloading process. On the occasion of the first three charge transfers, one electron each is transported three times from the skewed cubic $Mn_3CaO_4(H_2O)_2$ to reload $Mn^{(4)+}$, while it is likely for three protons to be dispatched from two of the hydroxy groups in the skewed cubic structure, $O^{(2)}H$ and $O^{(5)}H$, and from $Ca(H_2O)_2$. All these protons face the reaction field defined above. While the reloading dynamics is definitely needed, it is not stringently determined for protons to be dispatched in what order and how. The flexibility due to the presence of multiple channels of reloading processes should be good for the robustness of living bodies to cope with the fluctuations of nature.

(III) An oxygen molecule is formed after the fourth charge separation is over, the formation energy of which certainly compensates the energy demanded for isolation of four protons and four electrons from two water molecules. Obviously O=O formation is a result of the reloading processes and the reduction of $Mn^{(4)+}$, and thereby there can exist multiple mechanisms of formation depending on the history of reloading. The mechanisms also should depend on the timing for external water molecules to penetrate into the reaction field. We have proposed one possible mechanism of O_2 formation as a closing process of the catalytic cycle. It is quite likely that the mechanisms of O_2 formation proposed in the literature can be hardly justified if they have no causality with any dynamics of charge separation and reloading, even if they are correct in a pure chemistry context.

This work has been a direct extension of our building-block studies on water splitting dynamics starting from mononuclear and binuclear Mn oxo complexes to a tetranuclear Mn oxo complex. It has been observed before that mononuclear Mn oxide alone can work as a unit of both photoinduced and collision-induced ground-state charge separation. Besides, a water splitting catalytic cycle can be constructed in terms of even the mononuclear Mn oxo complex with additional equipment of buffers of electron and protons. As for the binuclear Mn oxo complex, no such external buffers are required to make a catalytic cycle, aside from the efficiency, since one of the two Mn atoms can work as a partial buffer.[22] Based on these insights, we now can comprehend (at least partly) how nature makes good use of the tetranuclear complex $Mn_3Ca(H_2O)_2(OH)_4$–OH–$Mn^{(4)}(H_2O)_2$: (1) it has an asymmetric binuclear structure, which is what we the call 3 + 1 structure, in which the "3" part corresponds to $Mn_3Ca(H_2O)_2(OH)_4$ and "1" represents $Mn^{(4)}(H_2O)_2$. The latter serves as an electrode providing both electrons and protons by the mechanism of coupled proton electron-wavepacket transfer (CPEWT) to the Y-shaped acceptors. The former serves as storage (magazine) of three electrons and three protons, which are sent off to reload the electrode part, that is, the "1" part. Therefore there is no need to prepare buffers of electrons and protons outside the Mn complex. (2) To let the electrode and the acceptors of electrons and protons keep to work, the relative positions of them are weakly fixed.[2] (3) The molecular structure of the "3" part is maintained not only by a μ-oxo bridge but by the carboxy groups. The presence of the carboxy groups covering the "3" part tends to prevent it from being accessed by external water molecules. However, the tetranuclear complex has a reaction field in between the "3" and "1" parts, in which to decompose water molecules as described above. For these reasons, the tetranuclear complex must have been far more efficient in evolution.

In this study we could perform real-time nonadiabatic electron wavepacket dynamics only for the four charge separation dynamics. As for the reloading processes, the active space for SA-MCSCF to treat all the Mn atoms on an equal footing was too huge to do so. Instead, we figured out an alternative method to track *ab initio* molecular dynamics with the use of UHF, the paths of which encounter nonadiabatic crossings. Development of a methodology of electron wavepacket dynamics for a huge active space is a future challenge. For the time being, an energy diagram of the proposed subprocesses has been examined semiquantitatively. We admit that we have a lot more to do for more accurate numerical studies.

Open Access Article. Published on 30 March 2020. Downloaded on 2/8/2026 12:45:32 PM.
This article is licensed under a Creative Commons Attribution 3.0 Unported Licence.

Thus, the focus of the present study has been placed on the very basic understanding of the role of $Mn_4Ca(OH)_5(HCOO)_5(H_2O)_4$ in water splitting. Yet, further elaboration of the model may be needed to match all the experimental findings thus far reported in the literature, and such sophistication of the model must be useful to design a battery of the mechanism proposed here.

Conflicts of interest

There are no conflicts of interest to declare.

Acknowledgements

This work was supported by JSPS KAKENHI (grant number JP15H05752). The computations were partly performed at the Research Center for Computational Science, Okazaki, Japan.

References

1 P. E. Siegbahn, *Acc. Chem. Res.*, 2009, **42**, 1871–1880.

2 Y. Umena, K. Kawakami, J.-R. Shen and N. Kamiya, *Nature*, 2011, **473**, 55–60.

3 M. Suga, F. Akita, K. Hirata, G. Ueno, H. Murakami, Y. Nakajima, T. Shimizu, K. Yamashita, M. Yamamoto, H. Ago and J.-R. Shen, *Nature*, 2015, **517**, 99–103.

4 M. Suga, F. Akita, M. Sugahara, M. Kubo, Y. Nakajima, T. Nakane, K. Yamashita, Y. Umena, M. Nakabayashi, T. Yamane, T. Nakano, M. Suzuki, T. Masuda, S. Inoue, T. Kimura, T. Nomura, S. Yonekura, L.-J. Yu, T. Sakamoto, T. Motomura, J.-H. Chen, Y. Kato, T. Noguchi, K. Tano, Y. Joti, T. Kameshima, T. Hatsui, E. Nango, R. Tanaka, H. Naitow, Y. Matsuura, A. Yamashita, M. Yamamoto, M. Yabashi, T. Ishikawa, S. Iwata and S. Jian-Ren, *Nature*, 2017, **543**, 131–135.

5 I. D. Young, M. Ibrahim, R. Chatterjee, S. Gul, F. D. Fuller, S. Koroidov, A. S. Brewster, R. Tran, R. Alonso-Mori, T. Kroll, T. Michels-Clark, H. Laksmono, R. G. Sierra, C. A. Stan, R. Hussein, M. Zhang, L. Douthit, M. Kubin, C. de Lichtenberg, L. Vo Pham, H. Nilsson, M. H. Cheah, D. Shevela, C. Saracini, M. A. Bean, I. Seuffert, D. Sokaras, T.-C. Weng, E. Pastor, C. Weninger, T. Fransson, L. Lassalle, P. Bräuer, P. Aller, P. T. Docker, B. Andi, A. M. Orville, J. M. Glownia, S. Nelson, M. Sikorski, D. Zhu, M. S. Hunter, T. J. Lane, A. Aquila, J. E. Koglin, J. Robinson, M. Liang, S. Boutet, A. Y. Lyubimov, M. Uervirojnangkoorn, N. W. Moriarty, D. Liebschner, P. V. Afonine, D. G. Waterman, G. Evans, P. Wernet, H. Dobbek, W. I. Weis, A. T. Brunger, P. H. Zwart, P. D. Adams, A. Zouni, J. Messinger, U. Bergmann, N. K. Sauter, J. Kern, V. K. Yachandra and J. Yano, *Nature*, 2016, **540**, 453–457.

6 J. Kern, R. Chatterjee, I. D. Young, F. D. Fuller, L. Lassalle, M. Ibrahim, S. Gul, T. Fransson, A. S. Brewster, R. Alonso-Mori, R. Hussein, M. Zhang, L. Douthit, C. de Lichtenberg, M. H. Cheah, D. Shevela, J. Wersig, I. Seuffert, D. Sokaras, E. Pastor, C. Weninger, T. Kroll, R. G. Sierra, P. Aller, A. Butryn, A. M. Orville, M. Liang, A. Batyuk, J. E. Koglin, S. Carbajo, S. Boutet, N. W. Moriarty, J. M. Holton, H. Dobbek, P. D. Adams, U. Bergmann, N. K. Sauter, A. Zouni, J. Messinger, J. Yano and V. K. Yachandra, *Nature*, 2018, **563**, 421–425.

7 J. Yano and V. Yachandra, *Chem. Rev.*, 2014, **114**, 4175–4205.

8 M. Askerka, G. W. Brudvig and V. S. Batista, *Acc. Chem. Res.*, 2016, **50**, 41–48.

9 S. Mauthe, I. Fleischer, T. M. Bernhardt, S. M. Lang, R. N. Barnett and U. Landman, *Angew. Chem., Int. Ed.*, 2019, **58**, 8504–8509.

10 Y. Zhang, D. Masuzaki and F. Mafuné, *Chem. Commun.*, 2019, **55**, 14327–14330.

11 X. Liu, A. L. Sobolewski, R. Borrelli and W. Domcke, *Phys. Chem. Chem. Phys.*, 2013, **15**, 5957–5966.

12 W.-J. Ong, L.-L. Tan, Y. H. Ng, S.-T. Yong and S.-P. Chai, *Chem. Rev.*, 2016, **116**, 7159–7329.

13 R. Welsch, E. Driscoll, J. M. Dawlaty and T. F. Miller III, *J. Phys. Chem. Lett.*, 2016, **7**, 3616–3620.

14 J. Ehrmaier, M. J. Janicki, A. L. Sobolewski and W. Domcke, *Phys. Chem. Chem. Phys.*, 2018, **20**, 14420–14430.

15 E. J. Rabe, K. L. Corp, A. L. Sobolewski, W. Domcke and C. W. Schlenker, *J. Phys. Chem. Lett.*, 2018, **9**, 6257–6261.

16 X. Pang, C. Jiang, W. Xie and W. Domcke, *Phys. Chem. Chem. Phys.*, 2019, **21**, 14073–14079.

17 K. Yamamoto and K. Takatsuka, *ChemPhysChem*, 2015, **16**, 2534–2537.

18 K. Yamamoto and K. Takatsuka, *Chem. Phys.*, 2016, **475**, 39–53.

19 K. Yamamoto and K. Takatsuka, *ChemPhysChem*, 2017, **18**, 537–548.

20 K. Yamamoto and K. Takatsuka, *Phys. Chem. Chem. Phys.*, 2018, **20**, 12229–12240.

21 K. Yamamoto and K. Takatsuka, *Phys. Chem. Chem. Phys.*, 2018, **20**, 6708–6725.

22 K. Yamamoto and K. Takatsuka, *J. Chem. Phys.*, 2020, **152**, 024115.

23 S. Hammes-Schiffer, *Chem. Rev.*, 2010, **110**, 6937–6938.

24 S. Hammes-Schiffer and A. A. Stuchebrukhov, *Chem. Rev.*, 2020, **110**, 6939–6960.

25 S. M. Lang, T. M. Bernhardt, D. M. Kiawi, J. S. Bakker, R. N. Barnett and U. Landman, *Angew. Chem., Int. Ed.*, 2015, **54**, 15113–15117.

26 Data provided by Prof. Fumitaka Mafune in private communication prior to publication.

27 T. Lohmiller, V. Krewald, A. Sedoud, A. W. Rutherford, F. Neese, W. Lubitz, D. A. Pantazis and N. Cox, *J. Am. Chem. Soc.*, 2017, **139**, 14412–14424.

28 A. Migliore, N. F. Polizzi, M. J. Therien and D. N. Beratan, *Chem. Rev.*, 2014, **114**, 3381–3465.

29 K. Nagashima and K. Takatsuka, *J. Phys. Chem. A*, 2012, **116**, 11167–11179.

30 L. W. Chung, S. Hayashi, M. Lundberg, T. Nakatsu, H. Kato and K. Morokuma, *J. Am. Chem. Soc.*, 2008, **130**, 12880–12881.

31 K. Yamamoto and K. Takatsuka, *J. Phys. Chem. A*, 2019, **123**, 4125–4138.

32 P. E. M. Siegbahn, *Chem. – Eur. J.*, 2006, **12**, 9217–9227.

Open Access Article. Published on 30 March 2020. Downloaded on 2/8/2026 12:45:32 PM.
This article is licensed under a Creative Commons Attribution 3.0 Unported Licence.

33 P. E. M. Siegbahn, *Biochim. Biophys. Acta*, 2013, **1827**, 1003–1019.
34 P. E. M. Siegbahn, *Proc. Natl. Acad. Sci. U. S. A.*, 2017, **114**, 4966–4968.
35 H. Isobe, M. Shoji, J.-R. Shen and K. Yamaguchi, *Inorg. Chem.*, 2016, **55**, 502–511.
36 M. Shoji, H. Isobe, J.-R. Shen, M. Suga, F. Akita, K. Miyagawa, Y. Shigeta and K. Yamaguchi, *Chem. Phys. Lett.*, 2019, **730**, 416–425.
37 M. Suga, F. Akita, K. Yamashita, Y. Nakajima, G. Ueno, H. Li, T. Yamane, K. Hirata, Y. Umena and S. Yonekura, *et al.*, *Science*, 2019, **366**, 334–338.
38 K. Takatsuka, *J. Phys. Chem. A*, 2007, **111**, 10196–10204.
39 T. Yonehara and K. Takatsuka, *J. Chem. Phys.*, 2008, **129**, 134109.
40 T. Yonehara, K. Hanasaki and K. Takatsuka, *Chem. Rev.*, 2012, **112**, 499–542.
41 K. Takatsuka, T. Yonehara, K. Hanasaki and Y. Arasaki, *Chemical Theory Beyond the Born-Oppenheimer Paradigm: Nonadiabatic Electronic and Nuclear Dynamics in Chemical Reactions*, World Scientific, Singapore, 2015.
42 H.-D. Meyer and W. H. Miller, *J. Chem. Phys.*, 1979, **70**, 3214–3223.
43 D. A. Micha, *J. Chem. Phys.*, 1983, **78**, 7138–7145.
44 A. Garca-Vela, R. Gerber and D. Imre, *J. Chem. Phys.*, 1992, **97**, 7242–7250.
45 W. H. Miller, *Faraday Discuss.*, 1998, **110**, 1–21.
46 M. D. Hack, A. W. Jasper, Y. L. Volobuev, D. W. Schwenke and D. G. Truhlar, *J. Phys. Chem. A*, 2000, **104**, 217–232.
47 K. Takatsuka, T. Fueno and K. Yamaguchi, *Theor. Chim. Acta*, 1978, **48**, 175–183.
48 R. S. Mulliken, *J. Chem. Phys.*, 1955, **23**, 1833–1840.
49 P.-O. Löwdin, *J. Chem. Phys.*, 1950, **18**, 365–375.
50 L. I. Schiff, *Quantum mechanics*, McGraw-Hill, New York, 1968.
51 K. Nagashima and K. Takatsuka, *J. Phys. Chem. A*, 2009, **113**, 15240–15249.
52 M. Okuyama and K. Takatsuka, *Chem. Phys. Lett.*, 2009, **476**, 109–115.
53 I. Barth, H.-C. Hege, H. Ikeda, A. Kenfack, M. Koppitz, J. Manz, F. Marquardt and G. K. Paramonov, *Chem. Phys. Lett.*, 2009, **481**, 118–123.
54 J. Manz, J. F. Pérez-Torres and Y. Yang, *J. Phys. Chem. A*, 2014, **118**, 8411–8425.
55 T. Bredtmann, D. J. Diestler, S.-D. Li, J. Manz, J. F. Pérez-Torres, W.-J. Tian, Y.-B. Wu, Y. Yang and H.-J. Zhai, *Phys. Chem. Chem. Phys.*, 2015, **17**, 29421–29464.
56 M. Okuyama and K. Takatsuka, *Bull. Chem. Soc. Jpn.*, 2012, **85**, 217–227.
57 D. J. Diestler, D. Jia, J. Manz and Y. Yang, *J. Phys. Chem. A*, 2018, **122**, 2150–2159.
58 R. Matsuzaki and K. Takatsuka, *J. Comput. Chem.*, 2019, **40**, 148–163.
59 R. Matsuzaki and K. Takatsuka, *J. Chem. Phys.*, 2019, **150**, 014103.
60 M. W. Schmidt, K. K. Baldridge, J. A. Boatz, S. T. Elbert, M. S. Gordon, J. H. Jensen, S. Koseki, N. Matsunaga, K. A. Nguyen, S. Su, T. L. Windus, M. Dupuis and J. A. Montgomery, *J. Comput. Chem.*, 1993, **14**, 1347–1363.
61 M. S. Gordon and W. S. Michael, *Theory and Applications of Computational Chemistry: the first forty years*, Elsevier, Amsteldam, 2005.
62 W. J. Stevens, M. Krauss, H. Basch and P. G. Jasien, *Can. J. Chem.*, 1992, **70**, 612–630.
63 B. O. Roos, P. R. Taylor and P. E. M. Siegbahn, *Chem. Phys.*, 1980, **48**, 157–173.
64 H. J. A. Jensen and H. Ågren, *Chem. Phys.*, 1986, **104**, 229–250.
65 ESI†.